Journal of Asian Earth Sciences 277 (2025) 106376

Contents lists available at ScienceDirect

Journal of Asian Earth Sciences

journal homepage: www.elsevier.com/locate/jseaes

Evaluating interseismic deformation patterns in the North Tabriz Fault (Iran) using enhanced fitting of velocity field and analysis of surface deformation

Milad Salmanian[a,*], Asghar Rastbood[b], Masoud Mashhadi Hossainali[a]

[a] Faculty of Geodesy and Geomatics Engineering, K. N. Toosi University of Technology, Tehran, Iran
[b] Department of Geomatics Engineering, Faculty of Civil Engineering, University of Tabriz, Tabriz, Iran

ARTICLE INFO

Keywords:
Creep and deformation
Inverse and forward problems
Boundary element method
Interseismic slip rate
Correlation and distribution
MCMC
North Tabriz Fault

ABSTRACT

Understanding the mechanisms and locations of interseismic strain accumulation along faults is essential for assessing earthquake hazards. However, the mechanical response during the transition from deep fault locking to creep behavior remains uncertain. Estimating the slip deficit within these transition zones is challenging. This study challenges the assumption of a constant depth distribution of interseismic slip rate along the fault over time and proposes variable locking depths as an alternative model. By rejecting the constant locking depth assumption, singularity issues during stress theorem resolution are resolved. To address this, we employ a methodology considering creep propagation within a fully elastic medium. This approach incorporates long-term deformation resulting from viscoelastic flow in the upper mantle and lower crust. Including viscoelastic effects improves the fit to interseismic deformation rates, yielding lower locking depths compared to fully elastic models. To conduct the investigation, the GPS velocity field is recovered using the forward problem and the boundary element method. Subsequently, a physics-based inversion approach, deep interseismic creep, is employed to determine interseismic deformation patterns on a strike-slip fault. Furthermore, this study examined the correlation between the dislocation parameters and their relationship, as well as established the probability distributions associated with each faulting parameter. This research highlights the importance of considering variable locking depths in understanding interseismic strain accumulation and the transition to creep behavior along faults. The findings contribute to improved earthquake hazard assessment and mitigation strategies by providing valuable insights into fault behavior mechanics along the North Tabriz Fault.

1. Introduction

Given that earthquakes originate from the sudden release of elastic strain along fault interfaces, obtaining reasonable approximations of the slip deficit and consequent strain accumulation assumes paramount importance for earthquake hazard evaluation. Despite notable progress in comprehending the mechanisms and locations involved in the accumulation of interseismic strain along faults, which enables the identification of fault segments with a higher propensity for earthquake occurrence, the mechanical response during the transition from deep fault locking to creep behavior remains uncertain. The precise estimation of the slip deficit within such transition zones is notably complex.

The acquisition of geodetic measurements that are both spatially and temporally dense is of great significance in the study of fault mechanics, specifically about the rheological and frictional properties along seismically locked fault segments (Bürgmann 2018; Fialko 2006). These measurements help in the comprehension of seismic and aseismic slip behaviors throughout different phases of the earthquake cycle (Aslan et al. 2019; Garthwaite et al. 2013; Hussain et al. 2018), as well as in the assessment of spatio-temporally variable seismic hazards. The temporary manifestation of surface deformation following a significant earthquake is well acknowledged in tectonically active regions across the globe. The utilization of spatial geodetic methods has enhanced our understanding of surface displacement (rates) at various spatial and temporal scales. Postseismic deformation signals can be discerned above the background noise associated with interseismic deformation patterns, with postseismic trends observed over timeframes ranging from days to decades (Nijholt et al. 2021).

---

* Corresponding author.
E-mail address: iammiladsalmanian@gmail.com (M. Salmanian).

https://doi.org/10.1016/j.jseaes.2024.106376
Received 16 May 2024; Received in revised form 28 September 2024; Accepted 18 October 2024

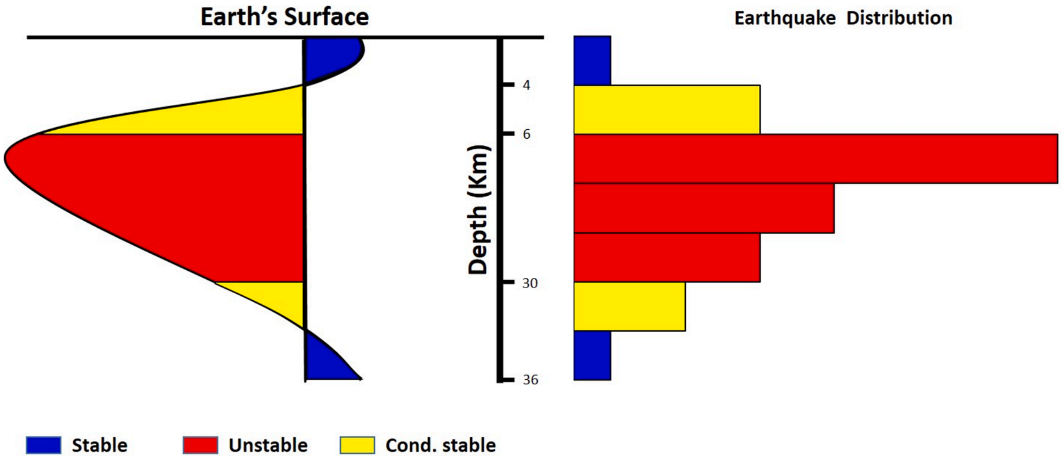

Fig. 1. Diagram illustrating the relationship between fault stability and depth for crustal faults and subduction zones, modified from (Scholz 1998). Earthquakes tend to initiate and propagate in unstable or locked regions. Conditionally stable areas may experience rupture due to adjacent earthquakes but are not typically sites for earthquake cores. Stable zones move with vibrations, effectively inhibiting rupture propagation.

Table 1

Earthquake focal mechanisms data in the investigated region. This table provides information gathered from two reputable sources, GCMT and IRSC. The data pertains to the area situated near the fault north of Tabriz in northwestern Iran, encompassing a latitude range of 37° to 39° and a longitude range of 45° to 47°.

Number	Origin Time And Location Parameters						Nodal Plane 1			Nodal Plane 2			reference
	Date	Time	Latitude (°N)	Longitude (°E)	Depth (Km)	Mw	strike (°)	dip (°)	rake (°)	strike (°)	dip (°)	rake (°)	
1	20,050,926	18:57:11.9	37.36	47.77	19.8	5.2	194	43	55	57	56	118	CMT
2	20,080,902	20: 0:54.5	38.69	45.79	15.4	5.0	113	80	−179	23	89	−10	CMT
3	20,120,811	12:23:15	38.393	46.806	9.0	6.5	267	81	−175	176	85	−9	IRSC
4	20,120,811	12:23:20.9	38.31	46.80	15.0	6.5	175	81	6	84	84	170	CMT
5	20,120,811	12:34:34	38.394	46.814	4.0	6.3	7	57	21	265	72	146	IRSC
6	20,120,811	12:34:39.5	38.35	46.78	19.2	6.4	10	50	36	255	63	134	CMT
7	20,120,811	15:21:14	38.427	46.800	4.0	4.8	266	79	174	357	84	11	IRSC
8	20,120,811	15:43:19	38.461	46.737	7.4	4.9	35	57	67	253	39	121	IRSC
9	20,120,811	22:24: 6.1	38.35	46.73	27.4	5.2	345	59	1	254	89	149	CMT
10	20,120,811	22:24:02	38.434	46.752	4.0	5.2	82	89	−165	352	75	−1	IRSC
11	20,120,813	1:56:10	38.418	46.692	3.9	4.7	261	80	178	352	88	10	IRSC
12	20,120,814	14:02:25	38.503	46.810	7.4	5.1	92	83	−176	1	86	−7	IRSC
13	20,120,815	17:49:04	38.440	46.670	4.0	4.9	80	70	165	175	76	20	IRSC
14	20,120,815	17:49:08.8	38.39	46.71	13.2	5.0	246	50	133	10	56	51	CMT
15	20,120,816	17:14:14	38.540	46.770	10.0	4.8	256	84	165	348	76	6	IRSC
16	20,120,816	17:14:17.8	38.35	46.81	25.2	4.8	263	78	172	355	82	12	CMT
17	20,121,107	6:26:31	38.458	46.565	10.0	5.7	272	75	−173	181	84	−15	IRSC
18	20,121,107	06:26:33.3	38.40	46.61	15.0	5.6	183	83	7	92	83	173	CMT
19	20,121,116	3:58:25	38.480	46.570	10.0	4.8	195	67	1	104	89	157	IRSC
20	20,121,116	03:58:28.4	38.49	46.66	15.8	4.8	109	81	179	199	89	9	CMT
21	20,121,223	6:38:57	38.487	44.934	12.0	5.0	70	68	149	172	62	25	IRSC
22	20,130,126	15:10:49	38.361	46.837	6.0	4.9	9	72	37	267	55	158	IRSC
23	20,130,126	15:10:52.8	38.37	46.87	21.6	4.8	269	66	163	6	74	25	CMT
24	20,130,418	10:39:37	38.430	45.360	6.0	4.9	204	83	28	110	62	172	IRSC
25	20,130,418	10:39:41.5	38.38	45.39	20.4	4.9	114	61	155	217	68	32	CMT
26	20,130,927	10:02:43	37.330	44.940	7.0	4.5	196	43	16	94	79	132	IRSC
27	20,131,108	10:12:34	37.800	47.170	9.0	4.4	311	79	−173	220	83	−11	IRSC
28	20,160,622	16:56:58	38.50	44.86	4.0	4.3	304	88	−166	214	76	−2	IRSC
29	20,170,827	23:14:52.6	37.87	47.14	17.5	5.0	116	72	−177	26	87	−18	CMT
30	20,191,107	22:47:05	37.71	47.52	8.0	5.9	307	86	−164	216	74	−4	IRSC
31	20,191,108	13:51:45	37.74	47.40	8.0	4.5	109	78	−161	15	72	−13	IRSC
32	20,191,110	2:13:45	37.67	47.47	7.0	4.4	81	54	102	241	37	74	IRSC
33	20,220,921	17:57:58.2	38.41	45.09	21.2	5.0	309	53	173	43	84	38	CMT
34	20,221,005	0:21:32.4	38.41	45.11	26.2	5.7	299	63	174	31	84	27	CMT
35	20,221,005	13:51:42.9	38.43	45.17	33.0	4.8	200	82	−1	290	89	−172	CMT

A fundamental representation of fault behavior is illustrated in Fig. 1, which categorizes the fault into three distinct regions: stable, conditionally stable, and unstable. The unstable section of the fault, which corresponds to the presently locked zone, is where earthquake nucleation occurs, characterized by a gradual accumulation of stress during the interseismic period. In contrast, the stable regions experience slippage manifested as seismic activity, allowing for long-term displacement without significant stress build-up. The delineation between these two regions, referred to as conditional stability, presents challenges; it is posited that a portion of long-term displacement transpires within these areas, yet the stress state remains largely undefined. Fig. 1 further illustrates the distribution of earthquake depths, as detailed in Table 1, indicating a predominant concentration of seismic events within the currently locked zone. (Fichtner et al. 2013) developed a full waveform inversion technique that integrates seismic data across a wide range of spatio-temporal scales. This approach enhances our understanding of the intricate details of crustal and upper mantle structures, as well as the interactions within the crust and the mantle that influence the dynamics of plate tectonics.

During the initial stages of investigating interseismic deformation, fault representation in models typically involved a single screw displacement situated within an elastic half-space. This approach, as proposed by (Savage and Burford 1970), assumed the fault to be locked at a specific depth while maintaining a constant velocity. Nevertheless, the screw dislocation model's credibility is compromised by the existence of an infinite concentration of stress at the dislocation tip, resulting in a lack of physical plausibility. To surmount this constraint and attain a more accurate representation of fault behavior, it becomes imperative to construct models that integrate transitional regions connecting completely locked faults to regions exhibiting free creep. In practical applications, numerous interseismic slip rate inversions incorporate some form of smoothing or assume a linear progression from a locked fault to a creeping fault, as exemplified in investigations such as (Flück et al. 1997). The objective is to minimize stress singularities, regardless of whether the approach leads to a gradual or rapid elimination of such singularities. Despite the widespread utilization of these approaches, there remains a limited understanding of the physical properties governing these transition zones, as noted by (Bruhat 2020).

The inclusion of fully dynamic earthquake cycle simulations reveals a notable evolution of the lock-to-creep transition. Enhancing the dynamic attenuation behavior within the velocity-strengthening region can facilitate the propagation of dynamic rupture during the post-earthquake lock-to-creep transition, as demonstrated by (Jiang and Lapusta 2016). Quasidynamic simulations, which integrate thermal stress and investigate slow-slip events, have corroborated these findings by illustrating the gradual propagation of the slow-slip event zone within the locked region between major earthquakes (Segall and Bradley 2012). A novel methodology for quantifying the interseismic slip rate, which allows for upslope propagation of slip in the locked region, was introduced in a recent investigation conducted by (Bruhat and Segall 2017). This innovative model simplifies the portrayal of deep interseismic slip by considering a loaded fault that maintains a consistent slip rate at its lower slope terminus.

In the study conducted by (Bruhat and Segall 2017), the primary focus was on the propagation of creep within an exclusively elastic medium. However, (Bruhat 2020) delves into the examination of prolonged deformation caused by viscoelastic flow in the lower crust and upper mantle. The objective of this study, carried out by (Bruhat 2020), is to investigate several elastic and viscoelastic models to accurately describe horizontal surface rates. Specifically, the deep interseismic creep method entails the upward propagation of interseismic slip into the locked zone. This approach conceptualizes the region encompassing the rift and the ETS (episodic tremor and slip) region as a long-lasting quasi-static crack formed due to the constant slope constraint imposed by the ETS region's movement velocity. Building upon classical crack models of faults, a simple model is introduced to calculate the growth of the crack over time. Analytical expressions for crack stress drop, slip, and slip rate along the fault are derived from this model. By incorporating the latest advancements and considering the coupling between fault creep and viscoelastic effects, this research offers valuable insights into the behavior of deep interseismic creep and its impact on horizontal surface rates along the North Tabriz Fault (NTF).

In (Wang et al. 2023), data from near-fault waveforms, GNSS static displacements, and surface ruptures were utilized to constrain the dynamic model. The findings indicated that the initial stress accumulation within the Kahramanmaraş-Çelikhan seismic fault facilitates the successful activation of the East Anatolian Fault (EAF) and results in supershear rupture in the northeastern segment. The intricate geometry of the fault resulted in considerable fluctuations in the rupture propagation rate along the southeastern portion of the EAF, alternating between supershear and subshear conditions, which subsequently contributed to the unexpectedly intense ground motion observed.

The NTF has exhibited a lack of significant seismic activity since 1780, maintaining a state of quiescence for more than two centuries. Nonetheless, recent seismological investigations along the fault have revealed that a considerable number of shallow microseismic events are confined to depths ranging from 7 to 21 *km* (Moradi et al. 2011). The Tabriz city being close to the North Tabriz fault highlights the need to investigate how this fault interacts mechanically, to understand the risk of earthquakes in the city. Additionally, given that the NTF functions as a predominant strike-slip fault, particularly within the Tabriz region, the rate of uplift is substantially lower than the horizontal slip rate, rendering it negligible along the fault (Azad et al. 2015; Salmanian et al. 2024a). (Rizza et al. 2013) conducted a study using two techniques to measure how fast the North Tabriz fault is slipping. They found that when they used GPS stations, the fault was slipping at a rate of 7.3 $mm/year$ and that it was locked at a depth of 18.3 *km*, while radar interferometric analysis yielded a slip rate of 6.0 $mm/year$. Another study by (Djamour et al. 2011) estimated that the fault was slipping at 7.3 $mm/year$, and that it was locked at a depth of 16.6 *km*, using a different method called block modeling. Additionally, (Khodaverdian et al. 2015) created kinematic finite element modeling to study how the land surface moves in the Iranian plateau. They used information about the fault's shape, slip rates measured from geological and landform studies, and the movement of GPS stations during significant earthquakes. When they analyzed this data, they estimated that the North Tabriz fault was slipping at a rate of 5.8 $mm/year$.

(Karimzadeh et al. 2013) also employed a modeling approach based on the simple elastic failure of Interferometric synthetic aperture radar (InSAR) observations' short baselines over time, resulting in a proposed average slip rate of 8.7 $mm/year$ and locking depth of 16 *km* for the North Tabriz Fault. In a separate study conducted by (Hessami et al. 2003) in the northwestern region of the fault, situated to the west of Tabriz city, paleo-seismological methods were utilized to estimate the slip rate. The findings from various methods ranged from 3.1 $mm/year$ to 6.4 $mm/year$ and a locking depth of 18 *km*, presenting different slip rate estimates for this specific segment of the fault. Through these diverse approaches, researchers have contributed valuable insights into the slip rate estimates for the North Tabriz Fault, each using different observation techniques and modeling methods to shed light on this significant tectonic feature.

Another relevant study concerning the North Tabriz Fault that is examined in this research, is the investigation conducted by (Aghajany et al. 2017). In their study, the slip rate was estimated at 6.1 $mm/year$ by integrating InSAR, troposphere-corrected GPS, and accurate leveling data. The research also reported a locking depth of 13.4 *km*. In a subsequent study by (Haji-Aghajany et al. 2019), improvements in troposphere corrections and interferogram corrections were made. Using the first method (phase-to-height ratio), the slip rate was determined to be 7.6 $mm/year$, with a locking depth estimated at 15.6 *km*. The second method in this research utilized 3D ray tracing, resulting in an estimated slip rate of 5.6 $mm/year$ for the North Tabriz Fault. Additionally, the locking depth in the northern region of Tabriz was reported as 13.1 *km* using this method.

The Eastern Anatolian Fault zone, situated in eastern Turkey and near northwestern Iran, facilitates the majority of the tectonic movement between the Arabian plate and central Turkey's interior, exhibiting minimal visible deformation. The overall direction of slip in this region is crucial for evaluating the slip magnitude on the North Anatolian Fault. According to (Taymaz et al. 1991), the estimated slip rate for the Eastern Anatolian Fault zone is approximately 29 $mm/year$, with a range between 25 and 35 $mm/year$. In the research conducted by (Taymaz et al. 2022), the study identifies the optimal slip distribution patterns of finite faults located in the border regions of Turkey and Iran, specifically in Northwestern Iran and Eastern Turkey. The mechanisms of normal faulting and strike-slip faulting have been characterized for the observed

Table 2

Summary of the North Tabriz fault characteristics in a simplified scenario using average values. The table presents essential details, including fault segment name, UTM coordinates of starting points, strike and dip measurements, as well as fault length and width.

Section Number	$X_{\mathrm{UTM}}(m)$	$Y_{UTM}(m)$	Strike ($^\circ$)	Dip ($^\circ$)	Length (km)	Width (km)
1	528,493	4,255,466	120	90	200	10,000

earthquake doublet. This research further documents the propagation of complex coseismic rupture along fault planes near the Turkish-Iranian border, noting a maximum displacement ranging between 20 and 50 *cm* from the hypocentre to the surface. Additionally, it describes discrete fault fragments extending up to 15 *km* in depth, with coseismic slip reaching 15 *km* along the strike.

The study conducted by (Taymaz et al. 2021) presents the source mechanisms and rupture processes associated with the East Anatolian Fault Zone (EAFZ) in Turkey, based on an analysis of seismic waveforms and spatial geodetic observations. An assessment of interferometric synthetic aperture radar (InSAR) data reveals that left-lateral coseismic slip and considerable deformation occur over a distance of up to 20 *km* on either side of the fault, accompanied by notable post-seismic displacement. In the research conducted by (Liu et al. 2023), kinematic rupture models for the two events of the Kahramanmaraş Earthquake Doublet were developed within the left-lateral strike-slip fault zone of the East Anatolian Fault Zone (EAFZ). This was achieved by inverting comprehensive seismic and geodetic data, utilizing intricate finite segment fault models (5–6 segments) derived from satellite observations, and analyzing the patterns of displaced aftershocks.

In the present study, a combination of the forward problem and the inverse problem was employed to estimate the values of eight seismic deformation parameters (full rupture depth, elastic thickness, slip rate, seismic displacement, Maxwell relaxation time, uniform creep depth,

Table 3

The initial values essential for the Monte Carlo Markov chain process.

parameter	$D(km)$	$H(km)$	$v^{\infty}(mm/year)$	$c(m)$	$t_R(year)$	$d(km)$	$H_{creep}(km)$	$\alpha(mm/year)$
(Rizza et al. 2013)	14.9818	28.8926	6.7	3.015	136.3636	18.3	27.2109	29.0365
(Karimzadeh et al. 2013)	14.9818	28.8926	8.7	3.915	136.3636	16	27.2109	29.0365
(Hessami et al. 2003)	14.9818	28.8926	4.75	2.1375	136.3636	18	27.2109	29.0365
(Aghajany et al. 2017)	14.9818	28.8926	6.1	2.745	136.3636	13.4	27.2109	29.0365
(Djamour et al. 2011)	14.9818	28.8926	7.3	3.285	136.3636	16.6	27.2109	29.0365
(Haji-Aghajany et al. 2019)	14.9818	28.8926	5.6	2.520	136.3636	13.1	27.2109	29.0365

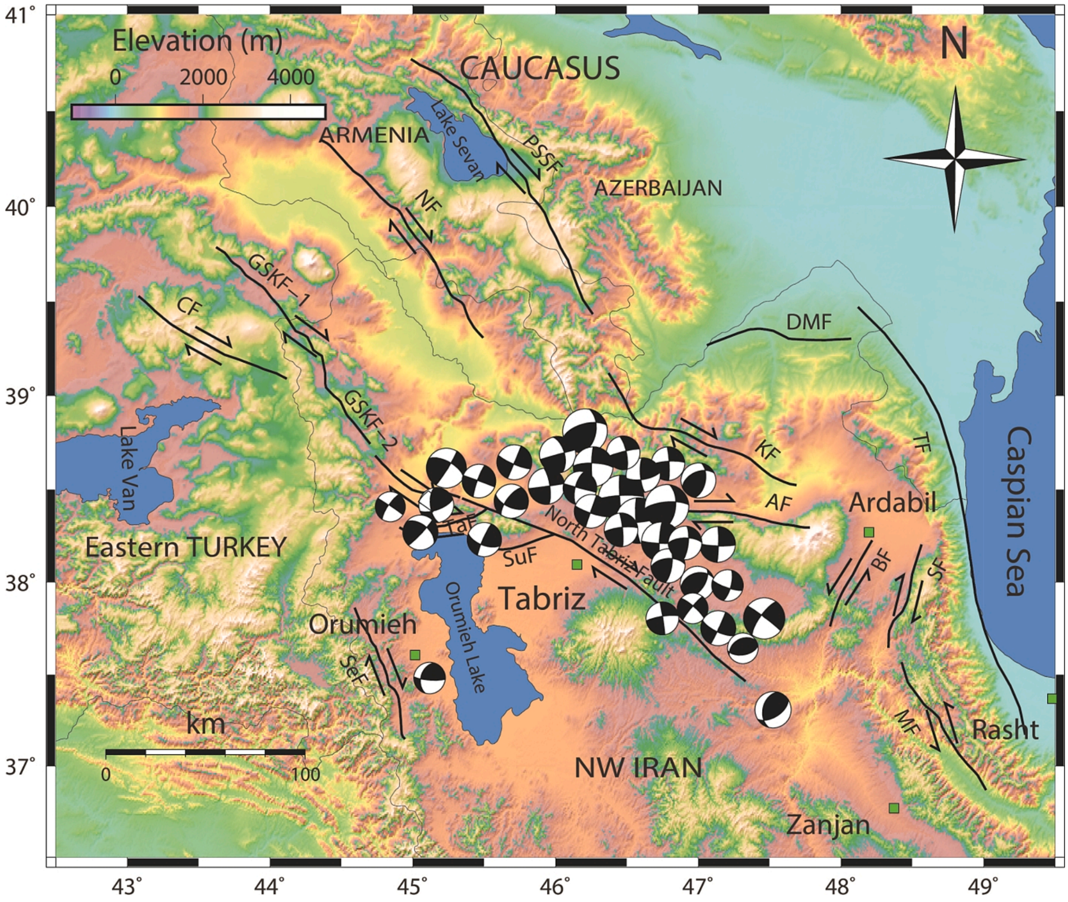

Fig. 2. Schematic view of the position of Tabriz city and the North Tabriz Fault (NTF), along with seismicity and earthquake ($M_w \geq 4$) Source mechanisms of major events in the area. The figure displays seismic events with a magnitude greater than 4 , recorded between 2005 and 2022, based on data from the Global Centroid Moment Tensor (GCMT) and between 2012 and 2019, based on data from the Iranian Seismological Center (IRSC). The fault lines shown in the illustration are indicated by black lines and were obtained from (Ambraseys and Melville 2005; Berberian 1994; Berberian and Yeats 1999).

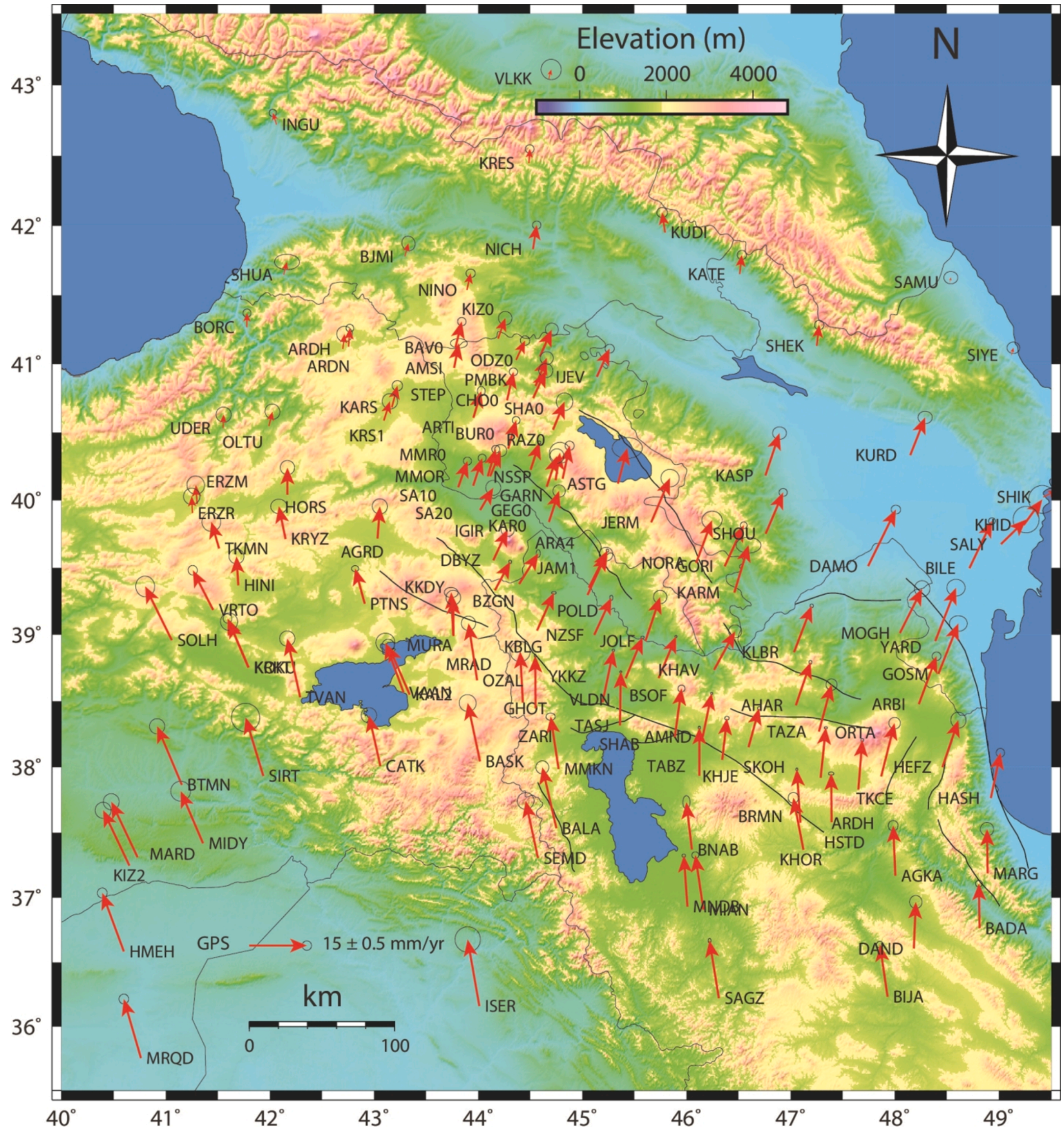

Fig. 3. Tectonic map of active faults in the northwestern region of Iran. This figure depicts the active faults in the northwestern region of Iran, revealing the tectonic deformation of the area through GPS velocity vectors represented by red arrows. The GPS velocity field data presented in this figure was sourced from (Khorrami et al. 2019). The observational GPS velocity field vectors used in this figure are referenced to a Eurasia-fixed frame. The fault lines shown in the illustration are indicated by black lines and were obtained from (Ambraseys and Melville 2005; Berberian 1994; Berberian and Yeats 1999). (For interpretation of the references to color in this figure legend, the reader is referred to the web version of this article.)

locking depth, and propagation velocity) for the North Tabriz Fault. The inverse problem was tackled using the Monte Carlo Markov chain tool, and to establish prior distributions for these eight target parameters and ensure comprehensive outputs, data from six previous research studies focused on determining the locking depth and slip rate of the North Tabriz Fault were selected. The findings of each of these six studies were utilized in the forward and inverse problems, and the results were compared to obtain a comprehensive estimation for all eight parameters. The locking depth and slip rate values obtained from these six previous studies are presented in Table 3.

2. Tectonic setting

Iran is located in a region where the Arabian and Eurasian tectonic plates collide at an oblique angle, leading to significant deformation within the continent. The majority of Iran's continental crust originated from a period of significant igneous activity that occurred during the Ediacaran and Early Cambrian epochs, approximately 600 to 500 million years ago. This geological event is referred to as the Cadomin orogeny in the context of Western Europe (Garfunkel 2015). Recent paleoseismic investigations have revealed the occurrence of several significant earthquakes along notable strike-slip faults traversing central Iran. These findings suggest that the region does not operate exclusively as a rigid block (Foroutan et al. 2014). The geological configuration of Iran is predominantly shaped by this collision, where the convergence rate between the plates is approximately $22 \pm 2\ mm/year$. The northwestern region of Iran is actively involved in this convergence, contributing to a rate of approximately $8 \pm 2\ mm/year$ (Vernant et al. 2004). The overall convergence is distributed across various geological processes, including shortening in the Zagros Mountains, internal deformation primarily caused by strike-slip faults in central Iran, and shortening in the Alborz Mountains. These tectonic processes collectively contribute to the complex geological evolution of the region.

Iran shares a northwestern border with Turkey, where two significant geological features are present: the North Tabriz Fault and the Eastern Anatolian Fault, both of which are characterized as strike-slip faults and are key components of the region's tectonic framework. Since the Miocene, the northward convergence of tectonic plates has resulted in compressional and extensional tectonics, leading to the development of significant surface features in Turkey, such as faulting and orogeny (Wang et al. 2020). A study conducted by (McKenzie 1976) indicates that satellite imagery of eastern Turkey reveals a prominent strike-slip fault measuring approximately 550 *km* in length. This fault extends from the Gulf of Iskenderun to the North Anatolian Fault, with a strike orientation of 60° east. It facilitates the majority of tectonic movement between the Turkish and Arabian plates. According to (Hu et al. 2024; Jia et al. 2023; Zhang et al. 2023), on February 6, 2023, two significant earthquakes with magnitudes of 7.8 M_w and 7.6 M_w struck the East Anatolian Fault Zone (EAFZ) and the Sürgü-Çardak Fault Zone (SCFZ). These seismic events resulted in extensive destruction of structures and infrastructure across southeast-central Turkey and northern Syria, leading to the tragic loss of over 50,000 lives. A study conducted by (Confal et al. 2020) aimed to examine the impact of seismic anisotropy by inverting both synthetic and real datasets from the eastern Mediterranean region, characterized by oceanic, continental, and extinct subduction systems. This study utilized realistic seismic anisotropy models, which were informed by 3D mantle convection simulations and shear wave splitting observations, as a priori constraints. The findings indicated that, in eastern Anatolia, there are no high-velocity anomalies associated with slab-related processes stemming from continental collision and break-off.

The northwestern region of Iran, encompassing the North Anatolian Fault, the Eastern Anatolian Fault, and the Caucasus Mountains, lies at the convergence of the Arabian Plate, the Anatolian Plateau, and the Eurasian Plate, forming a complex and dynamic geological system (as represented in Fig. 2). This intricate interaction facilitates the transfer of a portion of the northward movement of the Arabian Plate to the Anatolian Plateau through the mentioned fault system (Jackson 1992). Additionally, the tilting of the collision zone in the Zagros Mountains results in the release of movement, facilitating the interaction between the shortening in the Caucasus and the right-lateral slip along the North Tabriz Fault (Jackson 1992). This complex geological setting plays a crucial role in shaping the tectonic activity and movement in the northwestern region of Iran, highlighting the significance of understanding its dynamics and implications. The significant magnitude and extended recurrence interval of earthquakes in the northwest Iran region suggest that these events can be categorized as normal intraplate seismic activity (Berberian and Yeats 1999). Furthermore, the seismic moment released by earthquakes in eastern Turkey and northwestern Iran indicates that the tectonic deformation in this area is predominantly aligned with coseismic slip (Jackson et al. 1997).

Fig. 2 presents earthquake focal mechanism data obtained from credible sources, specifically the Global Centroid Moment Tensor (GCMT) database spanning from 2005 to 2022, along with data from the Iranian Seismological Center (IRSC) covering the period from 2012 to 2019. The pertinent information is summarized in Table 1. This focal mechanism data pertains to seismic events with a magnitude of 4 or greater ($M_w \geq 4$). The geographic focus of the study is illustrated in Fig. 2. This figure illustrates the position of the North Tabriz Fault located in northwestern Iran. The region's geological characteristics indicate a significant likelihood of seismic activity, as evidenced by the frequency of earthquakes that have occurred in recent years. Additionally, this figure highlights the proximity of the Tabriz metropolitan area to the NTF fault, thereby underscoring the necessity of conducting a thorough investigation into the seismicity of the region.

The North Tabriz Fault is a complex geological setting situated in the northwestern region of Iran. This fault, spanning a length of approximately 150 km (and about 210 km when considering the North Mishu Fault as its northwestern continuation), initiates from the southern region of Marand and follows a northwest-southeast orientation, extending through the northern periphery of Tabriz city, and reaching near Bostanabad. Moreover, the mentioned fault is linked to an overturned fault zone from its northwest side, characterized by a west-southwest rotation in the northern area of Orumieh Lake, encompassing the Sufian Fault (SuF) and Tasuj Fault (TaF). On its southeastern extension, the North Tabriz fault connects with the North and South Bozgosh, Dozdozan, and South Sarab overturned fault zones, resulting in a complex structural configuration that alters to an east-northeast trend (Berberian and Yeats 1999). Fig. 3 displays the tectonic map depicting the North Tabriz Fault, accompanied by the observational GPS velocity vectors sourced from (Khorrami et al. 2019). These GPS velocity vectors serve to illustrate and characterize the deformation rate within the region.

In the initial seismic reports (Berberian and Arshadi 1976), the North Tabriz fault was initially identified as a steep reverse fault. However, upon the examination of aerial photographs, indications of right-lateral strike-slip displacement along this fault were highlighted. Subsequently, other researchers provided more compelling evidence by documenting the clockwise movement of waterways and other Quaternary geomorphological features along this fault on the ground (Hessami et al. 2003; Karakhanian et al. 2004). This accumulating evidence supports the understanding that the North Tabriz Fault exhibits characteristics of both reverse faulting and right-lateral strike-slip motion, underscoring the complex nature of its tectonic behavior. In accordance with the outcomes of the stress field inversion and following Anderson's theory of faulting, it is determined that the North Tabriz Fault exhibits characteristics of a right-lateral strike-slip fault (Salmanian et al. 2024b).

(Berberian 1997) conducted a division of the northern fault of Tabriz into multiple segments, totaling a length of 210 km. These divisions were determined based on the analysis of surface ruptures observed in historical earthquakes that occurred in 1780, 1721, and 1786. According to (Karakhanian et al. 2004) research, the geometry of this fault comprises unaligned segments arranged in linear steps. Among these segments, two main parts, one located east and the other west of Tabriz city, hold particular significance for estimating earthquake risk. The western part extends from the city of Sufian to Tabriz city, and it displays clear indications of waterway movements, implying the occurrence of right-lateral strike-slip motion along the fault. Moreover, clear indications of surface faulting arising from historical seismic events can be identified by examining the complex morphological and structural characteristics of the land and conducting investigations into the ancient seismic activities in this specific region (Hessami et al. 2003). The presence of these features offers valuable insights into the seismic activity and potential risks associated with this fault section.

3. Data

In this study, we employ the forward problem approach along with the three dimensional boundary element method to reconstruct the displacement field and velocity field data along a fault-perpendicular profile. During the reconstruction process, we take into account the slip rate and locking depth obtained from the six selected studies (refer to Table 3). To retrieve the GPS velocity field, we utilize the forward problem operation, which involves treating the entire North Tabriz Fault plane as a 1×1 grid (as a single entity). The specific geometric characteristics of the North Tabriz Fault, necessary for applying the forward problem technique and recovering the velocity field, are elaborated in Table 2.

In this research, it is imperative to take into account the initial values of 8 parameters subjected to inversion (full rupture depth, elastic thickness, slip rate, coseismic displacement, Maxwell relaxation time, uniform creep depth, locking depth, and propagation velocity). The slip rate and locking depth parameters have been examined in previous studies, while for the remaining parameters, the initial values essential for the Monte Carlo Markov chain process were determined, as presented in Table 3. Furthermore, taking into account the past seismic events in Tabriz, it is important to mention that the latest significant

Table 4
A priori bounds for MCMC inversions.

Parameter	Symbol	Minimum	Maximum
Maximum depth of full earthquake rupture,km	D	10	15
Long-term fault slip rate,$mm/year$	v^{∞}	3	12
Elastic thickness,km	H	23	100
Half-space relaxation time,$years$	t_R	0	500
Coseismic displacement,m	Δu	1	5
Present-day locking depth,km	d	D	H
Depth of constant creep,km	H_{creep}	d	H
Recurrence time,$year$	T	$\Delta u/v^{\infty}$	$\Delta u/v^{\infty}$
Propagation speed,$m/year$	v_{up}	$(d-D)/(T-237)$	$(d-D)/(T-237)$
Time since 1786 earthquake,$years$	t	237	237 (fixed)
Block motion,$mm/year$	α	none	none

earthquake occurred in 1786. As a result, the t component, which represents the time that has passed since the last major earthquake, was set to 237 years.

Furthermore, the earthquake recurrence time (T) in this investigation was established at 450 years, as determined through an averaging of previous research findings. Additionally, building upon the insights from (Bruhat 2020), the optimal fit is achieved when the seismic relaxation time (t_R) is equivalent to $1/3.3$ during the earthquake recurrence period ($t_R = T/3.3$). As a result, the seismic relaxation time was determined to be almost 136.3636 years. On the other hand, in accordance with the coseismic displacement formula, it equals the product of the slip rate observed throughout the seismic recurrence period ($c = v^{\infty} \times T$).

Table 4 provides a concise summary of the previous findings, presenting the preceding bounds for the mentioned 8 parameters.

Considering the young structure of the northwestern region's crust in Iran, particularly in the North Tabriz Fault zone, it is possible to establish a boundary about the elastic thickness of the region. The elastic thickness is strongly influenced by the thermal structure of the lithosphere, its thickness, and the coupling between the crust and mantle. Specifically, the lithosphere extends from the crust to a depth of 60 to 100 km, and the elastic thickness represents the estimated thickness of an elastic plate that can replace the lithosphere to investigate observed deformation. In young areas, the elastic thickness ranges from 20 to 30 km, while in older areas, it is typically 40 to 50 km. Given the youthful nature of the crust in northwestern Iran, an elastic thickness of approximately 20 to 30 km can be assumed. The free parameter value is determined to calculate the motion of the rigid block based on global values. Detailed information regarding the upper and lower limits, as well as initial values, for all parameters, is provided in Table 3 and Table 4.

4. Methodology

In the present study, two methodologies, namely the forward problem method and the inversion method, have been employed. The initial step involves the application of the forward problem, utilizing Okada's fundamental solution and the three dimensional boundary element method. The primary objective of this approach is to recover GPS velocities along a fault-perpendicular profile. Subsequently, the second phase entails the inversion process, which incorporates the Monte Carlo Markov chain tool and the physical approach of interseismic deep creep. The GPS velocities derived from the forward problem are utilized in the inverse problem to determine the values of eight interseismic deformation parameters within the North Tabriz Fault zone.

In this study, we generated the velocity field data along the profile perpendicular to the fault by utilizing slip rate data that have been employed in six previous studies. The slip rates in these studies were derived using the observational GPS velocity field, and we have applied the same slip rates for our analysis. To clarify, the observational GPS velocity field vectors used in previous research were employed to calculate the slip rates, which we have incorporated in this study to generate the velocity fields along the profile perpendicular to the fault. It is important to note that the observational GPS velocities are Eurasia-fixed. In the second stage of our study, during the inverse problem analysis, we require velocity field vectors that are fixed to the fault under investigation. This allows us to address corrections related to the Earth's sphericity and to perform three-dimensional adjustments, ultimately producing a GPS velocity field that exclusively reflects the fault's displacement. Thus, in the first stage of this study, we approached the forward problem using calculated slip rates from the GPS observational velocities to generate a fault-fixed GPS velocity field. This method not only takes into account the observational velocity field but also incorporates the necessary corrections mentioned earlier.

4.1. *Forward problem*

In the beginning stage of this research, we utilized the three-dimensional boundary element method, which was introduced by (Gomberg and Ellis 1994), to analyze the forward problem of the North Tabriz Fault. The reconstruction of the displacement field was carried out by capitalizing on the intrinsic characteristics of the North Tabriz fault, including dimensions such as length, width, dip, and strike (detailed in Table 2), as well as the slip rate and locking depth data obtained from the six selected studies. The reconstruction was performed within the framework of a fault-perpendicular cross-sectional profile, specifically focusing on the GPS velocity data.

Throughout this research, a model based on a uniform and elastic half-space was adopted. The geometric characteristics of the fault, along with the rheological parameters of the surrounding region, were gathered from diverse sources and treated as constant values for the analysis. The formulation of the boundary conditions was derived from the geometric features of the North Tabriz Fault, along with the slip rate and locking depth data acquired from previous research endeavors. As a result, vertical movement of the fault was constrained, while tangential movement was allowed without limitations.

By imposing these boundary conditions under various scenarios, the GPS velocity field was reconstructed along the vertical profile of the fault. The boundary element method was utilized for the recovery process, with Okada's analytical model providing the fundamental solution. The primary objective of employing the forward problem method was to obtain sufficient displacement vectors, eliminate secondary motions and displacements from the GPS velocity data, apply 3D corrections, account for earth sphericity corrections, incorporate corrections associated with the Eurasia fixity of vectors, and exclusively focus on fault-related displacements.

One of the goals of applying the forward problem is to eliminate additional motions that may be present in the observed GPS velocity field data. Since the observed GPS velocity field data is Eurasia-Fixed (as represented in Fig. 3), it may include displacements that are solely related to the fault. In this study, we concentrate on the movements associated specifically with the fault itself and the displacements that occur under the fault's locking depth. We aim to investigate the displacements caused by deep creep during the interseismic period. Given that GPS velocities are based on Eurasia-Fixed, they may also include lateral movements in addition to those displacements. Hence, the forward problem was employed to isolate and produce the displacements related specifically to the fault.

To simulate the displacements arising from slip rates and locking depths of the fault within this study, the analytical framework proposed by (Okada 1985) is adopted. The Okada model is constructed based on the principles of dislocation theory. Generally, the input parameters for the Okada model are categorized into two groups: physical and geometric parameters. The physical parameters incorporated in this model encompass the Lame coefficients μ and λ relevant to the region under

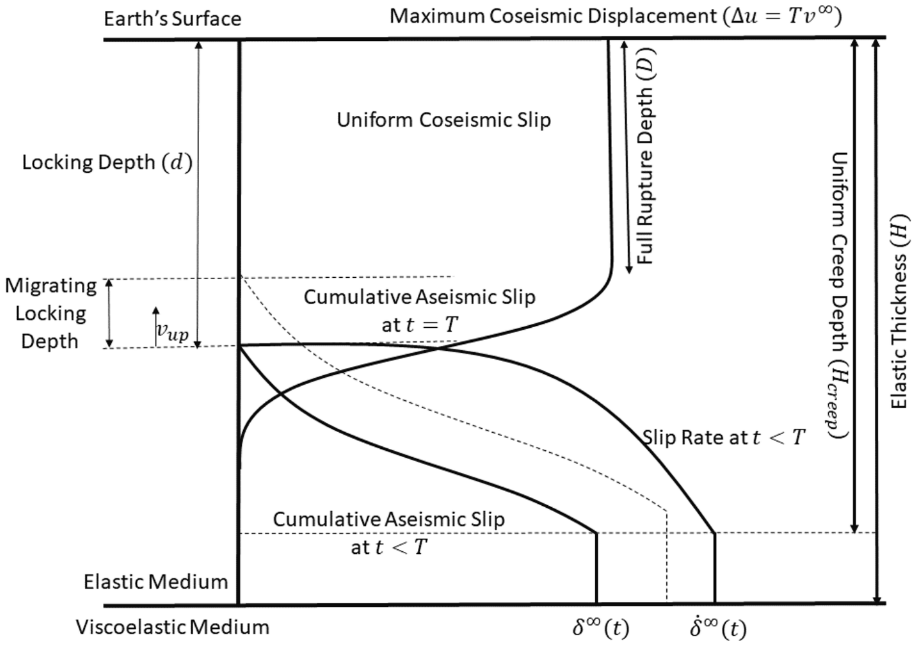

Fig. 4. Fundamental concepts underlying the deep interseismic creep approach.

investigation. These coefficients are ideally known, but if not available, the outcomes of sensitivity analyses of the Okada model may facilitate the utilization of globally averaged values.

The geometric parameters integrated into the Okada model encompass dimensions such as the length and width of the fault, locking depth, dip, strike, detachment rate, or slip rate. Additionally, the initial fault point's coordinates and the coordinates of observation points are also considered. Essentially, grounded in the fault's geometry and the underlying physical characteristics of the region, this model transforms fault displacement or slip rates into resultant displacement fields or velocity fields.

4.2. *Deep interseismic creep approach*

In the next stage of this research, the approach advanced by (Bruhat 2020) for assessing interseismic deformation rates through a viscoelastic earthquake cycle model was employed. This method encompasses the consideration of processes like the ascending propagation of profound interseismic creep. By using this method, eight distinct interseismic deformation parameters were determined within the context of the North Tabriz Fault system.

4.2.1. *Viscoelastic earthquake cycle model*

In this investigation, we examine a strike-slip fault situated within an elastic layer with a thickness represented as H, overlying a Maxwell's viscoelastic half-space. The fault, extending infinitely along the strike direction without variation, experiences periodic seismic activity every T years, leading to the fracturing of a segment. To ensure compatibility with the motion observed in distant regions, the highest coseismic displacement is defined as $\Delta u = Tv^{\infty}$, where v^{∞} denotes the enduring tectonic long-term plate movement rate. Fig. 4 illustrates the fundamental principles underlying the deep interseismic creep approach. In an elastic medium with a thickness of H and a viscoelastic half-space characterized by the Maxwell relaxation time t_R, long-term fault displacement occurs along the v^{∞} plane. Periodically, every T years, seismic events rupture the upper portion of the elastic crust. The maximum slip during an earthquake is determined by Tv^{∞}. The rupture pattern of the earthquake is initially uniform from the surface to a depth of D, after which it transitions into a conical shape. During the interseismic period, the deeper portion of the fault experiences creep, leading to an increase in the locking depth, d, at a rate of v_{up}. The interseismic slip gradually evolves from 0 at the depth of d to $\delta^{\infty}(t)$ at the depth of H_{creep}. Similarly, the creep rate transitions from 0 to $\dot{\delta}^{\infty}(t)$ at the depth of H_{creep}. Between the depths of H_{creep} and the elastic thickness H, both the creep and slip rates remain constant. It is important to note that the total seismic slip is consistent across all depths of plate movement. As creep penetrates the locked zone, stress concentrations are generated at the transition between velocity weakening and strengthening, which may initiate seismic events in that area. A comparable phenomenon has been documented in quasi-dynamical simulations incorporating thermal thrusting (Segall and Bradley 2012), where slow slip events progressively extend into the locked region that exists between megathrust earthquakes. The slow, yet significant, up-deep propagation of interseismic creep results in accelerated surface displacements. As the crack advances up-deep, both the slip rate and the acceleration profiles undergo temporal evolution.

Building upon the works of (Savage and Prescott 1978) as well as (Segall 2010), we examined the collective influence of periodically occurring sequences of K earthquakes at the instance $t_{eq} = -kT$, with k taking values within the range of $0.1.\cdots.K$. Subsequently, the resultant surface velocity v_i induced by seismic displacement δ_i between z_i and z_{i+1} is determined through the subsequent methodology:

$$v_i(x.t) = \frac{\delta_i}{\pi t_R} e^{-t/t_R} \sum_{n=1}^{\infty} \frac{G_n(x.z_i.H)}{(n-1)!} \sum_{k=0}^{K} e^{-kT/t_R} \left(\frac{t+kT}{t_R}\right)^{n-1} \tag{1}$$

in equation (1), t represents the duration elapsed since the occurrence of the previous seismic event, displaying positive values in the context of right-lateral strike-slip faults. The Maxwell relaxation time, denoted as t_R, about the viscoelastic substrate is ascertained through the relation $t_R = 2\eta/\mu$, wherein η signifies viscosity and μ signifies shear modulus. The amalgamated impact, designated as $v_{EQcycle}$, manifests as the seismic displacement arrangement elucidated by the δ_i distribution occurring at the depth $z = z_1.z_2.\cdots.z_i.\cdots.z_N$. This phenomenon is analogous to the depiction presented by (Bruhat 2020), as follows:

$$v_{EQcycle}(x.t) = \sum_{i=1}^{N} v_i(x.t) \tag{2}$$

4.2.2. Crack models for interseismic creep

Interseismic creep occurring beneath the depth at which locking transpires results in surface-level elastic distortion. In this section, we investigate the technique introduced by (Bruhat and Segall 2017) for characterizing profound interseismic creep. The scenario involves a vertically elongated $1D$ fissure of dimension a situated within the elastic layer, subjected to an upward displacement of magnitude δ^{∞} upon the viscoelastic medium. (Bruhat and Segall 2017) expanded the stress drop within the crack using Chebyshev polynomials of the first kind, denoted as T_i, as delineated subsequently:

$$\Delta T(\xi.t) = \mu \sum_{i=0}^{\infty} c_i T_i(\xi) \tag{3}$$

In equation (3), c_i signifies the coefficients linked with Chebyshev polynomials, while ξ stands as a spatial variable and $\xi \in [-1.1]$. It is explicitly expressed as $\xi = 1 - 2z/a$, wherein $z \in [0.a]$. This specification guarantees that the fixed state of the lower extremity of the underlying crack, situated at $z = 0$, remains upheld as the process of crack propagation unfolds. In this study, we employ the basic crack characterization outlined in (Bruhat and Segall 2017). This characterization entails a linear stress drop distribution along the crack. Nevertheless, it is noteworthy that the count of coefficients within the Chebyshev expansion is adjustable to accommodate distinct frictional characteristics, thereby enhancing the model's adaptability.

For the computation of elastic surface velocities resulting from profound interseismic creep spanning the extent of the fault length Λ, these equations are combined with Green's functions for a homogeneous half-space (G), as presented by (Bruhat 2020):

$$v_{elcreep}(x.t) = \int G(x.\xi)\dot{s}(\xi.t)d\xi \tag{4}$$

We discretize the Λ fault into distinct z_i and z_{i+1} segments, denoted by the indices $i = 1.2.\cdots.N$. This discretization allows for the discrete approximation of the aforementioned expression:

$$v_{elcreep}(x.t) \approx G\dot{s} \tag{5}$$

4.2.3. Viscoelastic response of time-varying interseismic creep

In this segment, we examine the technique introduced by (Bruhat 2020), designed to analytically compute the viscoelastic reaction resulting from varying slip rates over time within the completely locked region. The parameter $\dot{s}(t)$ indicates slip rate distribution within the region between the earthquake rupture depth D and the upper boundary of the viscoelastic layer H. Following the methods outlined by (Savage and Prescott 1978), along with (Segall 2010), the viscoelastic response linked with creep $\dot{s}_i(t)$ at a depth z_i is expressible as an infinite series of recurrent slip occurrences at time instances t' ranging from $-\infty$ to the present time t.

$$\widehat{v}_i(x.t.z_i) = \frac{1}{\pi} \sum_{n=1}^{\infty} \frac{G_n(x.z_i.H)}{(n-1)!} \int_{-\infty}^{t} \dot{s}_i(t')e^{-(t-t')/t_R} \left(\frac{t-t'}{t_R}\right)^{n-1} dt' \tag{6}$$

In equation (6), G_n is the spatial operator. The collective influence arising from the distribution of slip rates, characterized by the array of slip segments denoted as $\dot{s}_i$ lying between depths z_i and z_{i+1} for indices $i = 1.2.\cdots.N$, can be delineated as follows:

$$v_{vecreep}(x.t) = \sum_{i=1}^{N} \widehat{v}(x.t.z_i) \tag{7}$$

4.2.4. Slip rate inversion

The derived surface velocities, represented as V_{horz}, result from the combined effects of the viscoelastic earthquake cycle $V_{EQcycle}$ and the elastic and viscoelastic responses associated with interseismic creep, denoted as $V_{elcreep}$ and $V_{vecreep}$, respectively.

$$\begin{aligned} V_{horz} &= f\left(H, D, t_R, \ \Delta u, v_{\infty}, d, \ v_{up}, H_{creep}, \alpha\right) \\ &= V_{EQcycle} + V_{elcreep} + V_{vecreep} + \alpha + \varepsilon \, \text{with} \, \varepsilon \ N(0, \ \Sigma) \end{aligned}$$

Equation (8) introduces the parameter α, which characterizes reference frame offset or the difference between the fault model's reference frames (usually showing antisymmetry in fault cases) and the measured velocities. The free parameter, denoted as α, is employed to calculate the motion of the rigid block. The covariance matrix Σ, incorporates the statistical relationships among the variables present in the data.

The relationship between $V_{elcreep}$ and the slip rate vector $\dot{s}$, which remains unknown, is established using Green's functions G in a homogeneous elastic half-space. The objective of this research is to estimate several parameters using inversions. These parameters include the elastic thickness H, full rupture depth D, current location of the locking depth (indicated by the top of the creep zone) d, slip rate or long-term rate of plate motion v^{∞}, relaxation time of the viscoelastic medium t_R, and maximum coseismic displacement Δu, which is related to the recurrence time of earthquakes T. Moreover, an inversion is performed to estimate the depth at which the creep zone starts, H_{creep}, to consider the possibility of continuous movement at the transition between the elastic and the viscoelastic zones. It's important to mention that the fault maintains a consistent rate of slip $\dot{\delta}^{\infty}$ between depths H and H_{creep} (as represented in Fig. 4).

The slip patterns observed during earthquakes can be described in the following manner: From the surface of the Earth to a certain depth called the full rupture depth D, the slip distribution corresponds to the largest displacement experienced during the earthquake, Δu. To make sure that the total slip along the fault aligns with the maximum coseismic displacement at the end of an earthquake cycle, the slip distribution between the upper boundary of the area where slip occurs, d, and the lower boundary of that area, H_{creep}, is defined as the opposite of the slip distribution at the end of the cycle. This means that the way slipping occurs, denoted as $T = \Delta u / v^{\infty}$, is considered not just at the present moment but also throughout the entire cycle of the earthquake. Likewise, we determine the rate at which the rupture front propagates upward, v_{up}, by matching it with the slip in the elastic region, which is Δu at the end of the cycle. Furthermore, it is crucial for the region where slip occurs to extend down to the lower boundary of the earthquake zone by the completion of the earthquake cycle.

$$v_{up} = \frac{d-D}{T-237} \tag{9}$$

The main objective of this research is to create methods that can be used to evaluate different models of interseismic deformation. Some of these models take into consideration the propagation deep creep. In order to consider the viscoelastic deformation, we analyze seven parameters, including the full rupture depth (D), elastic thickness (H), viscoelastic relaxation time (t_R), coseismic displacement (Δu), long-term plate motion rate or slip rate (v^{∞}), and α, are incorporated into the calculations. When investigating models that involve propagation deep interseismic slip, an inversion is also conducted to determine the locking depth (d) and infer the propagation velocity of v_{up}. To carry out these inversions, we employ a technique known as Markov chain Monte Carlo (MCMC). MCMC algorithms help us estimate the most likely solution and create distributions that show the range of possible values. Depending on the particular inversions we conduct, we take into account prior knowledge about other parameters of the model. The details of the prior information constraints are provided in Table 4.

For each step of this study, a total of 1,000,000 simulations were performed using the Markov Chain Monte Carlo cycle. The input parameters of the model that exhibited the most variations among the six categories of input data while producing consistent outputs were related to the initial values and the upper and lower limits of parameters such as full rupture depth (D), elastic thickness (H), slip rate (v^{∞}), coseismic displacement (c), relaxation time (seismic rest period) (t_R), seismic

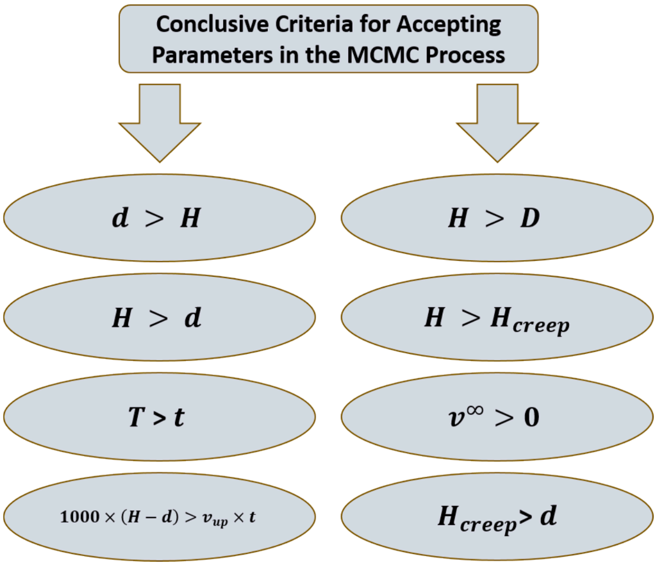

Fig. 5. Conclusive Criteria for Accepting Parameters in the MCMC Process.

recurrence or return period (T), locking depth (d), uniform creep depth (H_{creep}), and the free parameter for calculating the motion of the rigid block (α). The estimated values of locking depth and slip rate from the six previous studies, as presented in Table 3, displayed significant differences. In this study, the estimated values with these differences were used as initial values. However, the same upper and lower limits were applied to all parameters in all six categories. The seismic recurrence time from previous studies was averaged, and the seismic relaxation time was calculated based on this average. By combining the seismic return period and slip rate, the coseismic displacement was determined for the six sets of input data.

Fig. 5 shows the final eight criteria for accepting target parameters during each iteration of the Markov chain Monte Carlo. These criteria are represented in accordance with the concepts of the deep interseismic creep approach depicted in Fig. 4.

5. Result

In order to enhance the reliability and comprehensiveness of the results, a total of six prior studies focused on the North Tabriz Fault were carefully chosen for this investigation. The outcomes of these selected studies serve as the input data for both the forward and inverse problems, thus enabling the analysis to be conducted using six distinct datasets. Consequently, six output categories were generated, and a systematic comparison was carried out to evaluate the consistency and implications of the findings.

In this research undertaking, we commence by employing the geometric parameters attributed to the North Tabriz fault, delineated in Table 2. Simultaneously, we incorporate the slip rate and locking depth data acquired from the six preceding studies, explicitly documented in Table 3. Our approach involves tackling the forward problem as the initial step. To resolve this, we implement the boundary element technique outlined by (Gomberg and Ellis 1994). Using this approach, we were able to accurately determine the distribution of GPS velocities across a profile perpendicular to the fault. The results of our analysis, which involved solving the forward problem, are presented visually in Fig. 6, showing the field vectors representing the GPS velocity.

In the next stage of our study, we take the GPS velocity vectors we obtained and use them as input for an inversion process. We utilize a physics-based approach that takes into account slipping occurring deep within the Earth's crust between earthquakes (interseismic creep), and we use a tool called Markov chain Monte Carlo. Through this process, we evaluate how well the geodetic rates align with the North Tabriz Fault for the six studies we previously identified. The results of this inversion procedure are summarized in Table 5. Within this table, the inversion results encompass a range of parameters. These results are derived from a comprehensive analysis based on one million simulations for each of the selected studies. Fig. 7 presents the posterior distributions of the output parameters, accompanied by the best-fit values of the parameters identified in (Aghajany et al. 2017). The posterior distribution figures for the remaining five studies are provided in Appendix 1. These figures include the correlation values of the output parameters, along with a corresponding color map representation for the parameters.

To attain an optimal assessment of the values about parameters full rupture depth (D), elastic thickness (H), slip rate (v^{∞}), coseismic displacement (c), relaxation time (t_R), locking depth (d), uniform creep depth (H_{creep}) and propagation velocity (v_{up}), a consolidation of outcomes from six precedent studies referenced in Table 5 is performed through averaging. The comprehensive presentation of results encompassing all eight parameters is illustrated in Table 6.

Figs. 7, 12, 13, 14, 15, and 16 present the posterior distributions of eight parameters across all six studies. It is evident from these figures that, although there are variations in the values of the input parameters among the six studies, the range of output values and the best-fit estimates across all repetitions remain largely consistent, exhibiting only minor discrepancies. Additionally, the correlation values of the eight parameters for the six studies are displayed, which generally fall within the range of -1 to 1. These correlation values are represented in the color map using a gradient from blue to yellow.

The correlation coefficient ranges from -1 to 1. A correlation value of 1 signifies a perfect direct relationship between two variables, indicating that an increase or decrease in one variable will result in a corresponding increase or decrease in the other. Conversely, a correlation value of -1 denotes a complete inverse relationship, where an increase in one variable is associated with a reduction in the other, and vice versa. A zero correlation suggests the absence of a linear relationship between the two variables. Consequently, the sign of correlation illustrated in Figs. 7, 12, 13, 14, 15, and 16 reflects the nature of the linear relationship between the parameters. In these figures, the color map in the first column demonstrates the correlation between the full rupture depth and parameters such as elastic thickness, slip rate, coseismic displacement, relaxation time, locking depth, uniform creep depth, and propagation velocity, respectively. Similarly, the color maps in the subsequent columns depict the correlation among other parameters relative to each other.

Fig. 8 illustrates the Probability Density Function (PDF) and histogram for eight specified parameters. The data utilized are derived from a comprehensive dataset encompassing six studies. This figure delineates the range through which each parameter varies throughout the inversion process. Furthermore, the distribution of each parameter is presented by established criteria and assessments. The histograms also display the values for the Akaike Information Criterion (AIC) and the Log-Likelihood (LL) of the data as two important criteria.

As illustrated in Fig. 8, the parameters elastic thickness (H), slip rate (v^{∞}), relaxation time (t_R), locking depth (d), uniform creep depth (H_{creep}), and propagation velocity (v_{up}) exhibit a Generalized Extreme Value (GEV) distribution. In contrast, the parameters of coseismic displacement (c) and full rupture depth (D) follow a Uniform distribution, indicating that within the specified interval, each parameter value has an equal probability of occurrence. The generalized extreme value distribution is commonly utilized to approximate the maxima of lengthy (finite) sequences of random variables and belongs to a family of distributions that are associated with extreme value theory. Specifically, the GEV distribution integrates the characteristics of the Gumbel, Fréchet, and Weibull distributions into a unified structure.

In the present investigation, by considering the optimal operational domain for each parameter within the framework of this physical

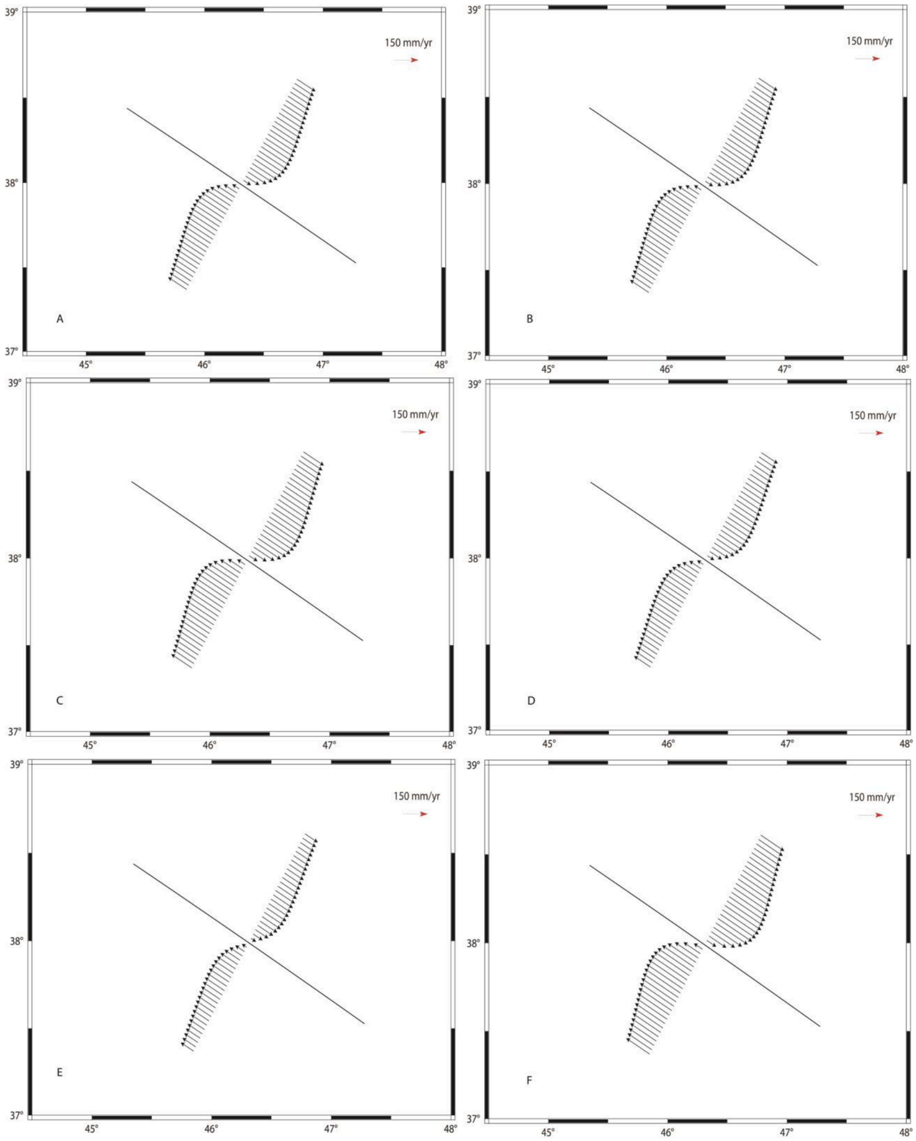

Fig. 6. GPS velocities reconstructed along the perpendicular profile of the North Tabriz fault employing the slip rate approximated in the investigation by A: (Rizza et al. 2013), B: (Djamour et al. 2011), C: (Haji-Aghajany et al. 2019), D: (Aghajany et al. 2017), E: (Hessami et al. 2003), and F: (Karimzadeh et al. 2013).

Table 5
The results of the best fit of the physical inversion for 8 parameters using the data of all six selected studies.

parameter	$D(km)$	$H(km)$	$v^{\infty}(mm/year)$	$c(m)$	$t_R(year)$	$d(km)$	$H_{creep}(km)$	$v_{up}(m/year)$
(Rizza et al. 2013)	14.6	23.1	4.7	4.98	192	14.9	22.1	0.389
(Karimzadeh et al. 2013)	14.7	23.2	5.82	4.55	119	14.8	23	0.137
(Hessami et al. 2003)	11.3	23	3.75	3.61	155	11.5	22.1	0.324
(Aghajany et al. 2017)	14.5	23.2	4.28	2.33	128	14.6	21.6	0.512
(Djamour et al. 2011)	12.7	23.1	5.34	4.36	156	12.9	20.8	0.419
(Haji-Aghajany et al. 2019)	12.3	23.2	4.42	2.27	100	12.3	21	0.0653

inversion process, it becomes feasible to offer commentary on the permissible range of values for each parameter. Within this inversion method, the inferred rupture depth falls within the range of 10 to 15 *km*. Evaluations of the elastic thickness exhibit a span extending from 22 to 38 *km*. Coseismic displacement is observed to span from 2 to 5 *m*. The temporal interval of recurrence time lies between 450 and 750 *years*. The slip rate is bounded between 3 and 6 $mm/year$, while the prevailing locking depth is identified in the range of 12 to 15 *km*, coinciding with the focal region of predominant microseismic activity. Lastly, rates about the gradual progression and expansion of creep (propagation velocity) encompass a spectrum ranging from 0 to 8.5 $m/year$. The period marked by seismic relaxation time displays variations spanning from 140 to 250 *years*.

The best-fitting models suggest that to align with the observed data, the propagation rates along the fault must be extremely low, specifically less than 1 $m/year$. Furthermore, the gap seems to function as a coherent zone where shear resistance diminishes with increasing slip. The phenomenon of up-dip propagation offers a credible rationale for the steep slip rate profile inferred for the North Tabriz fault, obviating the necessity for temporal variations in fault strength.

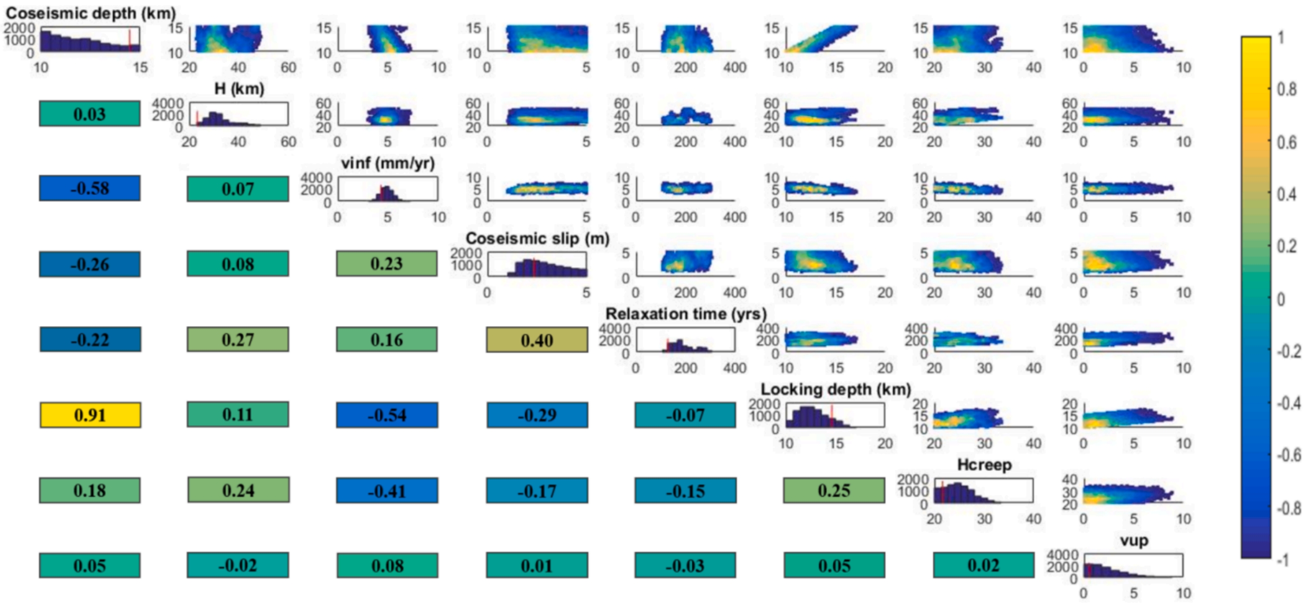

Fig. 7. Marginal posterior distributions and extracted correlation values for estimated parameters from combining the forward problem and propagating creep inversion process using (Aghajany et al. 2017) data. The best fit solution is shown with red lines. (For interpretation of the references to color in this figure legend, the reader is referred to the web version of this article.)

Table 6
Average values for 8 parameters resulting from applying physical inversion on data from previous studies.

parameter	$D(km)$	$H(km)$	$V^{\infty}(mm/year)$	$C(m)$	$t_R(year)$	$d(km)$	$H_{creep}(km)$	$v_{up}(m/year)$
value	13.35	23.13	4.72	3.68	141.67	13.5	21.77	0.308

6. Discussion

Earthquake risk assessment is fundamentally determined by both the size of the rupture zone and its proximity to population centers on land. The size of the rupture zone is directly related to the earthquake's magnitude, given that the seismic moment is proportional to the area of rupture. In subduction zone contexts, the distance from population centers is influenced by the maximum depth of the seismic event; deeper ruptures tend to produce greater slip at the surface due to the inclination of the fault interface. In the research conducted by (Melgar et al. 2020), a kinematic earthquake slip model was employed to analyze the most significant seismic event in the Eastern Anatolian Fault region over the past five decades. The findings indicate that the majority of slip occurrences are concentrated in three primary zones, with two regions exhibiting depths between 2 and 10 *km*, while a deeper slip zone extends to a depth of 20 *km*. For the North Tabriz Fault, as illustrated in Fig. 1, slip events predominantly manifest at depths ranging from 6 to 20 *km*. The inversion of interseismic geodetic deformation rates allows for the estimation of the locked section of the megathrust, with the down-dip limit designated as the locked depth. Below this threshold, the fault behaves seismically, and elastic strain may not accumulate. The locked depth is consequently utilized as an indicator of the maximum potential rupture depth, although it is important to note that it serves only as a lower limit for the maximum rupture area. The deep interseismic creep approach for crack propagation serves as an effective mechanism for identifying and characterizing potential non-stationary behaviors in surface deformation.

The deep interseismic creep approach necessitates the utilization of a prior distribution to infer the parameters. Within the study area of this investigation, substantial disparities were noted among the available values. As a consequence, the outcomes of six prior studies were treated individually, with consistent upper and lower limits applied to all six data categories. These limits were determined based on the geophysical characteristics specific to each parameter within the research area. The results of this investigation provide significant insights into the complex interrelationships between various geological parameters influencing fault behavior, specifically in the context of the North Tabriz fault. The observed correlation values and probability distributions indicate clear patterns that can be employed to enhance our understanding of seismic activity and fault mechanics.

While (Bruhat and Segall 2016) postulated that long-term rates are statistically independent, the presence of spatial correlations in geodetic data is well-established e.g., (Gudmundsson et al. 2002; Mavrommatis et al. 2015). This investigation entails the estimation of correlations among parameters to adequately account for their interrelationships. Based on Figs. 7, 12, 13, 14, 15, and 16, it is observed that the propagation velocity parameter exhibits the weakest correlation with other parameters. This can be attributed to the fact that this parameter is not directly incorporated into the inversion process; instead, it is derived from the calculated parameters after each cycle using Equation (9). One of the primary objectives of this study is to evaluate the propagation velocity within the framework of interseismic deep creep. Notably, the most robust correlation is found between the locking depth and the full rupture depth parameters. This relationship is aligned with the concept represented in Fig. 4 and Fig. 5, wherein the only distinction arises from the notion of variable locking depth. The correlation illustrated in the figures demonstrates a significant and pronounced correlation between the parameters of elastic thickness and uniform creep depth. As depicted in Fig. 4 and Fig. 5, the foundational elements of the study and the underlying physical model support the significant correlation and relational integrity of these two parameters. A similar conclusion holds for the correlation and strong relationship between locking depth and uniform creep depth. Consequently, it can be asserted that the color map and posterior distributions are entirely consistent with the physical model and are firmly grounded in the established foundations of the study.

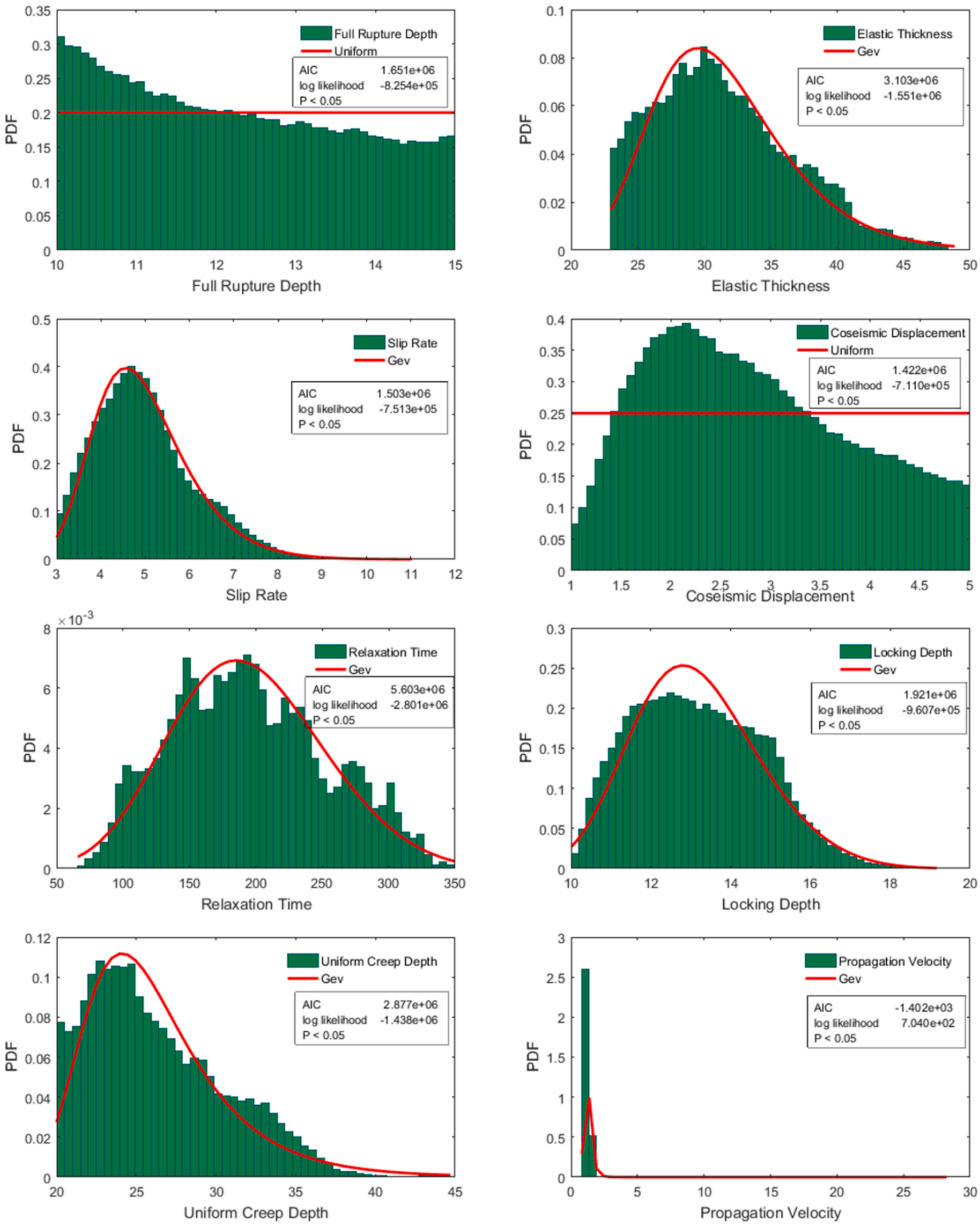

Fig. 8. Histogram and Probability Density Function (PDF) representing the output parameters derived from the combined data of six replicates. P-values demonstrate the Kolmogorov-Smirnov test statistic.

In ((Segall 2010), section 6), viscoelastic relaxation time is articulated as the ratio of parameter ζ to parameter μ, with ζ denoting viscosity and μ indicating shear modulus ($t_R = 2\zeta/\mu$). These parameters, when viewed through the spatial operators and Green's functions, exhibit interconnected relationships with elastic thickness. This interrelationship has subsequently resulted in an enhanced correlation between the viscoelastic relaxation time and elastic thickness parameters. The coseismic displacement is derived from the product of the seismic recurrence period and the slip rate ($c = v^{\infty} \times T$). Given that viscoelastic relaxation time is a fraction of the seismic recurrence period, variations in the correlation between the parameters of coseismic displacement, viscoelastic relaxation time, and slip rate can be attributed to this underlying relationship. Consequently, it can be inferred that the parameters of viscoelastic relaxation time and slip rate play a predominant role in the determination of the coseismic displacement parameter, respectively.

The analysis of the correlation presented in Figs. 7, 12, 13, 14, 15, and 16 indicates a negative correlation between full rupture depth and the parameters of slip rate, coseismic displacement, and Maxwell relaxation time. This suggests an inverse relationship wherein increased full rupture depth, particularly when it approaches the locking depth, corresponds to reduced values of the propagating locking depth. Consequently, the slip rate, coseismic displacement, and Maxwell relaxation time exhibit a decrease. The relationship $c = v^{\infty} \times T$ implies that the values of coseismic displacement and slip rate are intrinsically linked. Color correlation maps further reveal a significant inverse correlation between locking depth and both slip rate and coseismic displacement, indicating that a reduction in locking depth is associated

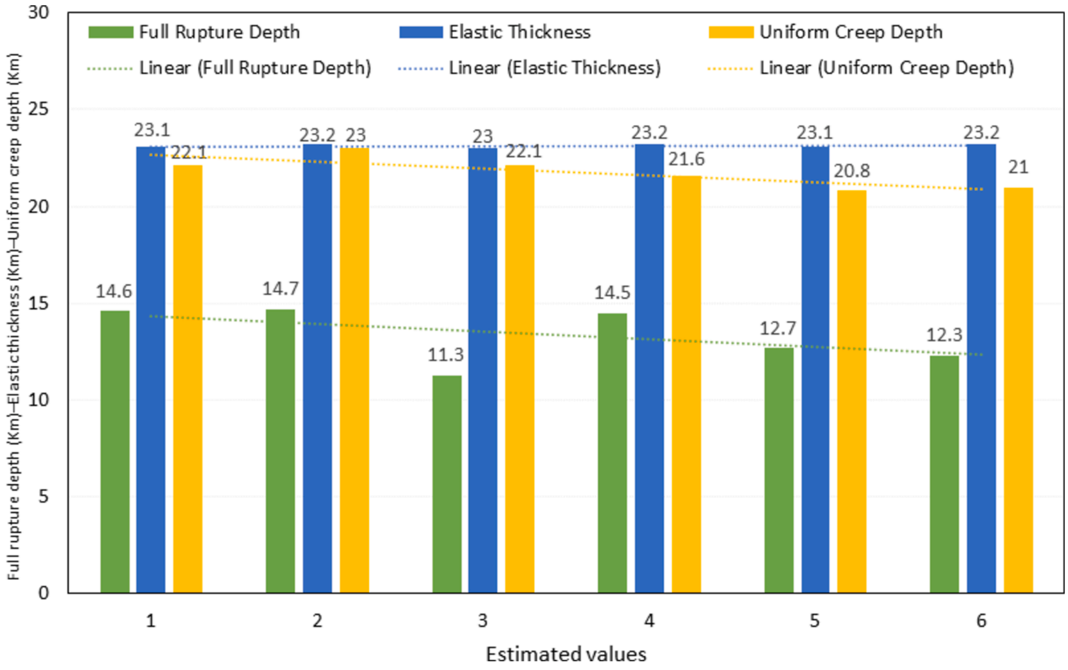

Fig. 9. Estimated values of full rupture depth, elastic thickness, and uniform creep depth using six datasets in the current study. The trend lines depict the average values and demonstrate the consistency of the outputs with the geophysical information of the study area.

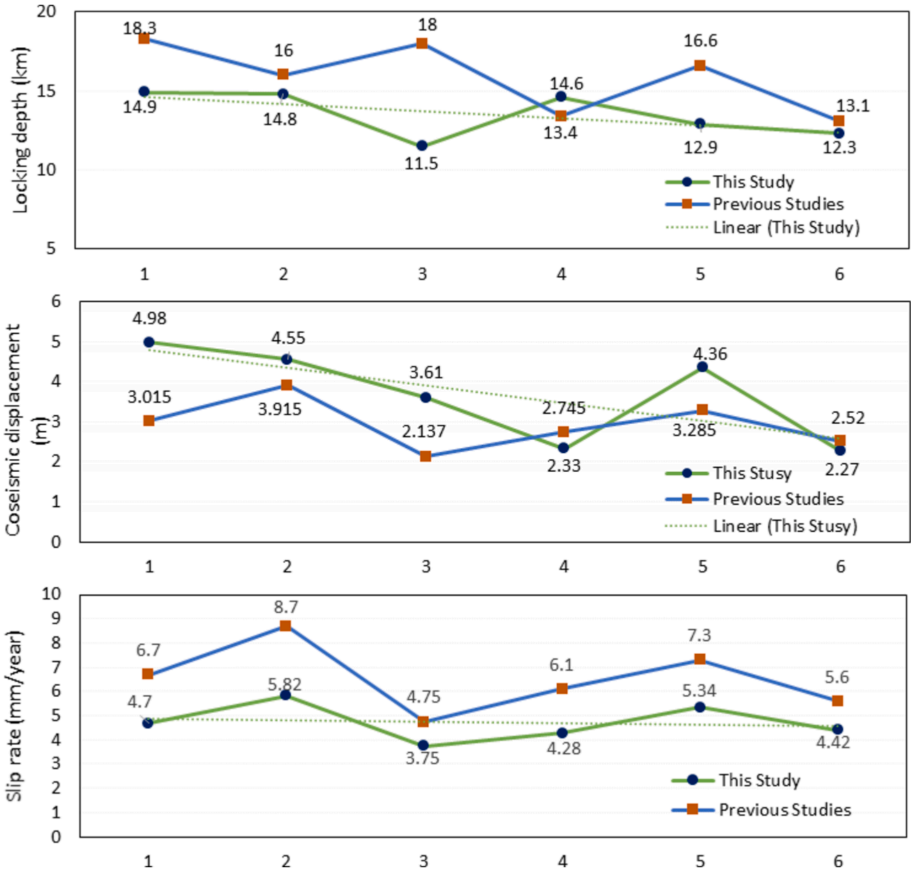

Fig. 10. Analysis of slip rate values, coseismic displacement, and locking depth estimation in this study using six datasets. The trend lines represent the average values for each parameter. The trend line for the slip rate parameter demonstrates the complete alignment between the slip rate obtained in this study and the slip rate derived from the paleoseismological method.

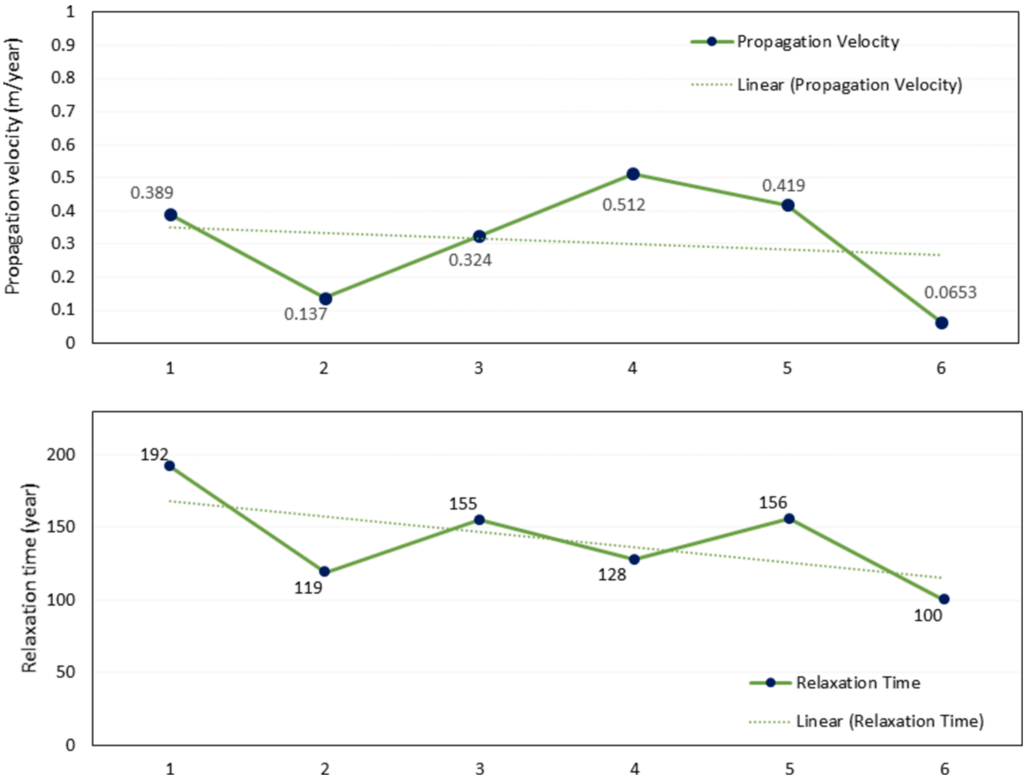

Fig. 11. Analysis of estimated parameters, including seismic relaxation time and propagation velocity, in this study. The trend lines represent the approximate mean values for each parameter.

with an increase in both the slip rate and coseismic displacement. This relationship is especially evident when contrasting the North Tabriz Fault with the San Andreas Fault; the locking depth of the North Tabriz Fault exceeds that of the San Andreas Fault, which has a locking depth of approximately 10 *km*. In comparison, the slip rate for the North Tabriz Fault is substantially lower than that of the San Andreas Fault, which exhibits a slip rate of around 34 *mm*/*year*. Consequently, the observed correlations and corresponding color maps align well with the geophysical characteristics and physical evidence associated with right-lateral strike-slip faults.

The analysis of various tests and criteria delineates the types of probability distributions associated with each parameter, as illustrated in Fig. 8. Furthermore, alternative distribution types are ranked for each parameter based on these criteria and their fit to the observed data. Following the uniform distribution, the full rupture depth (D) parameter exhibits the closest alignment to the generalized extreme value (GEV) distribution, ranked second in priority. Similarly, the coseismic displacement (c) parameter closely aligns with the Gamma distribution, while it ranks third in proximity to the GEV distribution. Other examined parameters also tend to follow the GEV distribution. Consequently, it can be concluded that all seismic deformation parameters investigated in the deep interseismic creep model, either conform to a GEV distribution or exhibit probability distributions that closely resemble it. The GEV distribution itself is characterized as a composite of Gumbel, Fréchet, and Weibull distributions. This finding is particularly noteworthy, as the GEV distribution is typically employed to model extreme values that arise from stochastic processes. The relevance of GEV distributions in geophysical contexts, especially in seismic studies, cannot be overstated; they help us understand the potential for extreme events based on historical data. The characteristics of the GEV distribution suggest that the peak values of these parameters are more pronounced than those predicted by a normal distribution, underscoring the importance of extreme values in seismic hazard assessments.

The inferred rupture depth is particularly significant as it aligns with the depth range commonly associated with active seismic events in subduction zones and continental fault systems. This depth also coincides with the average location of microseismic activity, which underscores the importance of the identified range. The alignment of this rupture depth with existing seismic data reinforces the notion that the physical inversion methodology employed provides reliable insights into the seismic characteristics of the region under investigation. In the northwest region of Iran's crust, as well as in the North Tabriz Fault zone, a youthful geological structure is observed. Young areas exhibit an elastic thickness ranging from 20 to 30 *km*, whereas older areas demonstrate an elastic thickness of 40 to 50 *km*. Notably, the elastic thickness values derived from this study, as depicted in Fig. 9 and Table 5, align precisely with these established concepts. Fig. 4 illustrates the fundamental principles underpinning the methodology employed in this investigation. It is observed that the locking depth should exceed the full rupture depth, the uniform creep depth should exceed the locking depth, and the elastic thickness should surpass the uniform creep depth. These conditions have been duly considered during the Monte Carlo Markov chain iterations to ascertain the acceptance of parameters. The resulting outputs, as illustrated in Figs. 9 and 10 and Table 5, demonstrate complete concordance with these underlying principles.

The slip rate, obtained from six different data categories, is depicted in Fig. 10, averaging 4.72 *mm*/*year* for the North Tabriz fault (refer to Table 6). This slip rate aligns completely with the slip rate derived from paleo-seismological methods (Hessami et al. 2003), which provide direct and realistic observations. Furthermore, it concurs entirely with the slip rate results obtained through (Salmanian et al. 2024a)'s boundary element method. In the present study, the coseismic displacement for the northern Tabriz fault is estimated to be 3.68 *m*, which is deemed suitable considering the regional slip rate and the duration of the seismic recurrence period. This slip rate reflects the long-term build-up of stress along the fault line, which is crucial for understanding the seismic cycle and predicting future seismic events. In particular, slip rates at the higher end of this range could lead to more frequent or intense seismic activity, warranting further investigation into the dynamics of stress accumulation and release in this region.

Coseismic displacement encompasses both dynamic and static components, occurring concurrently during fault rupture and being influenced by the same phase of each specific earthquake. Displacements at this scale have been recorded in major fault systems around the world, suggesting that the values inferred in this study may correspond to significant earthquake scenarios. These findings emphasize the relevance of monitoring and mitigating risks associated with such seismic activity, particularly in densely populated areas prone to earthquakes. The estimated locking depth in this study is lower than the values reported in previous studies (as shown in Fig. 10), averaging 13.5 km. A locked fault refers to a fault that remains immobile due to the frictional resistance surpassing the shear stress acting upon it. Within the deep interseismic creep approach, the estimated locking depth for the North Tabriz Fault is determined to be 13.5 km. This value adheres to the conditions stipulated in Fig. 4 and Fig. 5, being smaller than the elastic thickness yet greater than the full rupture depth. Notably, in the interseismic deep creep approach, the locking depth is not regarded as a fixed parameter but rather allowed to assume values ranging between the full rupture depth and the elastic thickness. The output value represents the model with the highest probability, thereby yielding the most optimal fit for the estimated locking depth. The coincidence of this locking depth with the focal region of significant microseismicity suggests that this area is crucial for understanding the mechanics of fault slip and the onset of larger seismic events.

The ETS zone is situated within a negative shear stress rate range, spanning from 30 to 45 km in depth. Given the preference for deeper locking depths in the data, the crack is confined to an area characterized by elevated long-term slip rates, specifically at depths of 20 to 30 km within the ETS region. Although the inversions do not impose restrictions on the mechanical behavior of this zone, they do affirm its creeping nature, with ETS events occurring in the deeper sections of the fault. Long-term deformation datasets can be characterized by the gradual up-dip progression of interseismic creep within the gap and ETS regions. As this creep extends into the locked zone in an up-dip direction, the resulting slip rate profile exhibits an increased gradient, leading to a higher slip rate relative to a static model.

Fig. 11 illustrates the seismic relaxation time, derived from the aggregation of various data sets. For the North Tabriz Fault, this cycle is estimated to have an average duration of 141.67 $years$, representing the period of post-seismic relaxation. By considering the duration of the seismic recurrence period, an estimation of the seismic relaxation time can be made. According to the study conducted by (Bruhat 2020), the best fit occurs when the seismic recurrence period is approximately 3.3 times the duration of the seismic relaxation time. Consequently, the estimated seismic recurrence period is calculated to be around 467.51 $years$, aligning with global average values and previously assumed averages for the North Tabriz Fault. This range suggests substantial accumulative stress before a significant fault slip might occur. It also highlights the importance of factoring in relaxation times when assessing regional seismic risk.

Another parameter evaluated in this modeling is the propagation velocity. In the context of the deep interseismic creep approach, the average propagation velocity for the North Tabriz Fault is determined to be 0.308 $m/year$ (refer to Table 6). Equation (9), coupled with the accepted parameter values, is employed to calculate the propagation velocity at the end of each cycle, thereby facilitating an assessment of the model and its results. The San Andreas Fault serves as a natural laboratory, and the propagation velocity for this fault is determined to be less than 1 $m/year$. Given that the North Tabriz Fault shares similar characteristics with the San Andreas Fault (right-lateral and strike-slip fault), it is expected to exhibit a lower propagation velocity because of the lower slip rate than the San Andreas Fault. The calculated propagation velocity for the San Andreas Fault is approximately 0.8 $m/year$, further supporting the reasonableness of the calculated propagation velocity of 0.308 $m/year$ for the North Tabriz Fault. As depicted in Fig. 11, the values of propagation velocity resulting from this approach, considering each data set, are found to be less than 1 $m/year$, indicating a lack of propagation. Furthermore, the range for the rates of creep propagation indicates variability in the fault's behavior and could illuminate the complex interplay between steady creeping motion and abrupt seismic events. The presence of creep suggests a certain level of aseismic displacement, which can relieve stress without resulting in an earthquake. However, the upper limit of this range, particularly, raises questions about the potential for large elastic rebounds that may occur should this creep behavior transition into more frequent seismic activity.

Dehydration reactions are believed to augment pore pressure while reducing effective normal stress within the episodic tremor and slip (ETS) region. Should a crack propagate upwards into an area of elevated effective normal stress, the velocity of propagation is anticipated to diminish. This suggests that deep interseismic creep may have advanced more rapidly through the rift and the ETS region in previous periods; however, current data are inadequate to validate this hypothesis. The physical model under consideration posits that a characteristic rupture occurs instantaneously on an annual basis. While it takes into account the cumulative response of the underlying viscoelastic medium to each characteristic earthquake, it overlooks the phenomena of afterslip and the broader postseismic deformations. Notably, postseismic slip can represent a substantial fraction of the displacement within the creeping zone. As the deeper segments of the elastic layer undergo postseismic slip, they further enhance the response of the viscoelastic medium. However, this additional time-dependent behavior associated with afterslip is entirely disregarded in the viscoelastic modeling of the deep interseismic creep approach.

The Eastern Anatolian Fault, located along the border between Iran and Turkey, is recognized as a significant tectonic feature characterized by its strike-slip mechanism. The methodology employed to integrate both forward and inverse analysis has been applied to the North Tabriz Fault, another critical tectonic entity exhibiting slip behavior in the area. In this study, we estimated the full rupture depth of the North Tabriz Fault to be 13.35 km, a finding that aligns with the values reported by (Taymaz et al. 2022) for the Eastern Anatolian Fault zone. Furthermore, the estimated rupture propagation speed in this investigation is 30 $cm/year$, which corroborates the rate reported for the eastern region of Turkey.

7. Conclusion

This study explores the interaction between slow-deforming layers and the time-dependent slip behavior in the interseismic period. In contrast to earlier assumptions, which posited a consistent coseismic displacement and a sudden halt of seismic activity at the full rupture depth, this study presents an actual transition zone beneath this depth. This enhancement enables the simultaneous propagation of sudden displacements during earthquakes and gradual slipping between events, offering a more comprehensive understanding of fault dynamics.

This investigation employed the boundary element method to address a forward problem, facilitating the reconstruction of velocity field vectors across a fault profile. The obtained velocity field was subsequently utilized in an inversion process based on the deep interseismic creep approach, which significantly enhances our comprehension of the spatial dynamics associated with the slip zone throughout the interseismic period, particularly at the interface between the locked zone and the upper region of the viscoelastic medium. The velocity field data were analyzed across six distinct datasets, involving one million simulations conducted via the deep interseismic creep approach, resulting in negligible variations in outputs and demonstrating convergence for all eight targeted parameters.

In this investigation, an approach grounded in physical principles is employed to concurrently determine the values of six parameters (full rupture depth (D), elastic thickness (H), coseismic displacement (c),

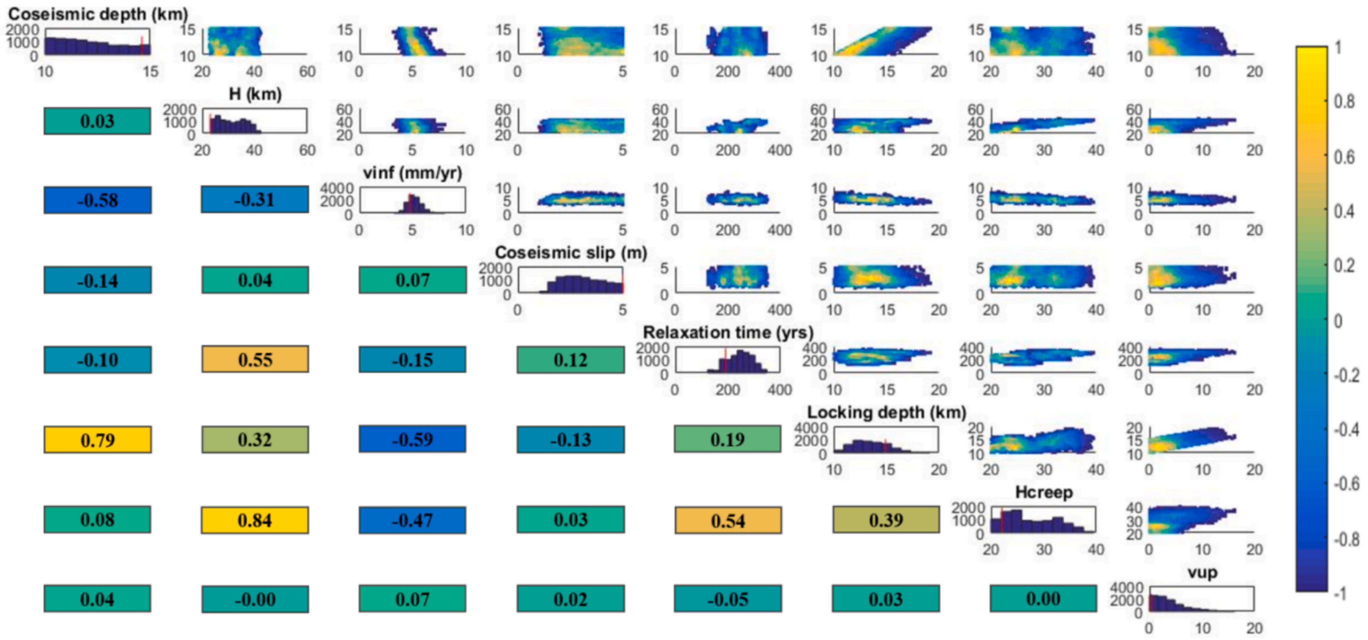

Fig. 12. Marginal posterior distributions and extracted correlation values for estimated parameters from combining the forward problem and propagating creep inversion process using (Rizza et al. 2013) data. The best fit solution is shown with red lines. (For interpretation of the references to color in this figure legend, the reader is referred to the web version of this article.)

relaxation time (t_R), uniform creep depth (H_{creep}) and propagation velocity (v_{up})) and two parameters related to slip rate (v^{∞}) and locking depth (d). This study marks the first instance where these parameters are jointly and simultaneously deduced for the North Tabriz Fault zone, representing an optimal fit for collective integration within an inversion process. The values obtained in this study derive their Reliability from their foundation in the initial values extracted from the slip rate and locking depth data originating from six prior studies. Moreover, an extensive investigative effort was undertaken to establish the preliminary values of the remaining six parameters. The findings of this study indicated that the majority of the Interseismic deformation parameters conform to the Generalized Extreme Value (GEV) distribution.

The results of this study not only enhance our understanding of the physical behavior of the North Tabriz Fault but also present a foundation for future research in seismic risk assessment. By elucidating the correlation of fault parameters and their distributions, this investigation paves the way for enhanced predictive models and better preparedness in the face of potential seismic threats. Future studies may build upon these findings to further delineate how these relationships manifest in different geological settings, ultimately leading to improved hazard mitigation strategies. By categorizing parameters into distinct statistical distributions, we pave the way for refined modeling techniques that can better capture the probabilities and mechanics of seismic events.

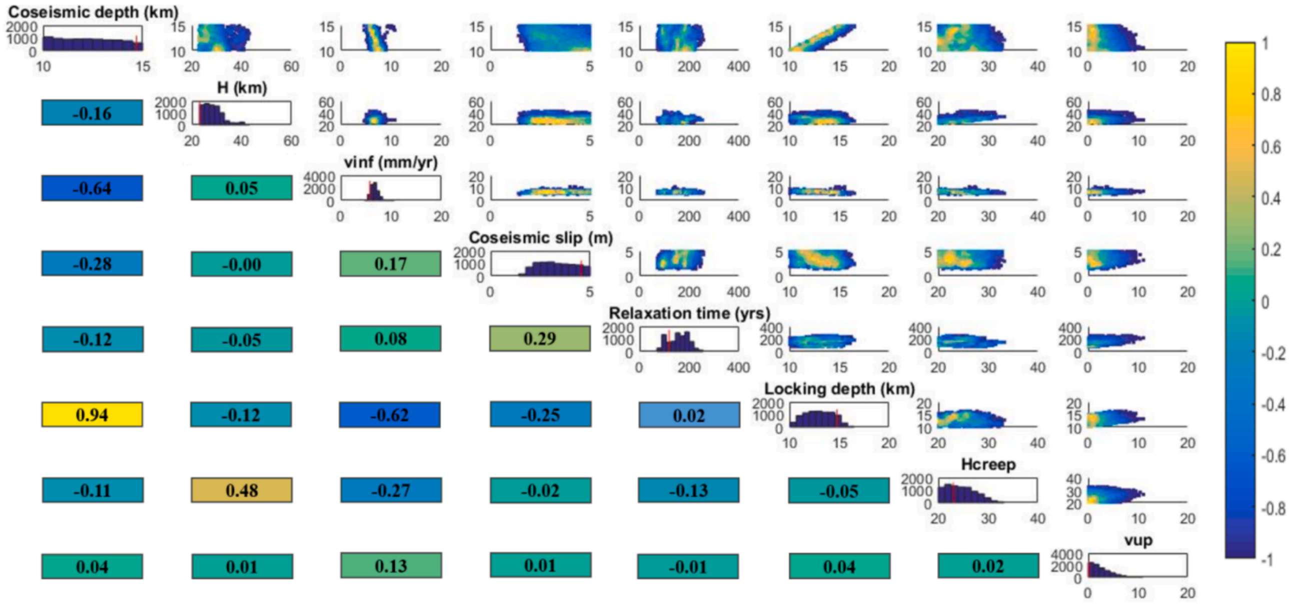

Fig. 13. Marginal posterior distributions and extracted correlation values for estimated parameters from combining the forward problem and propagating creep inversion process using (Karimzadeh et al. 2013) data. The best fit solution is shown with red lines. (For interpretation of the references to color in this figure legend, the reader is referred to the web version of this article.)

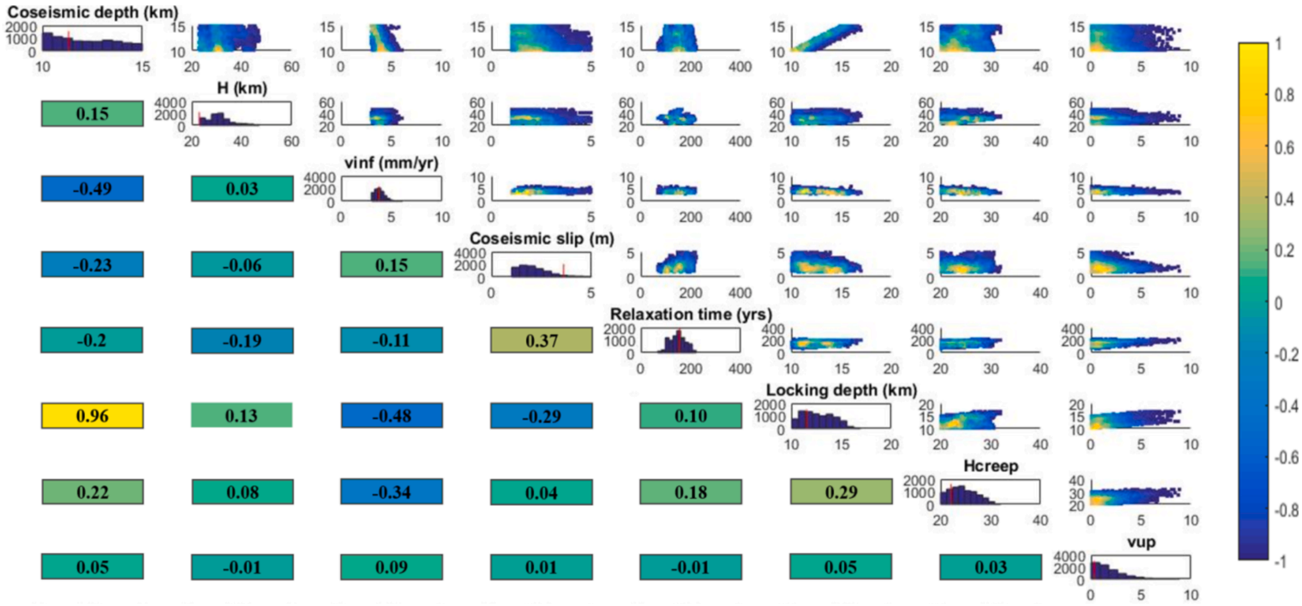

Fig. 14. Marginal posterior distributions and extracted correlation values for estimated parameters from combining the forward problem and propagating creep inversion process using (Hessami et al. 2003) data. The best fit solution is shown with red lines. (For interpretation of the references to color in this figure legend, the reader is referred to the web version of this article.)

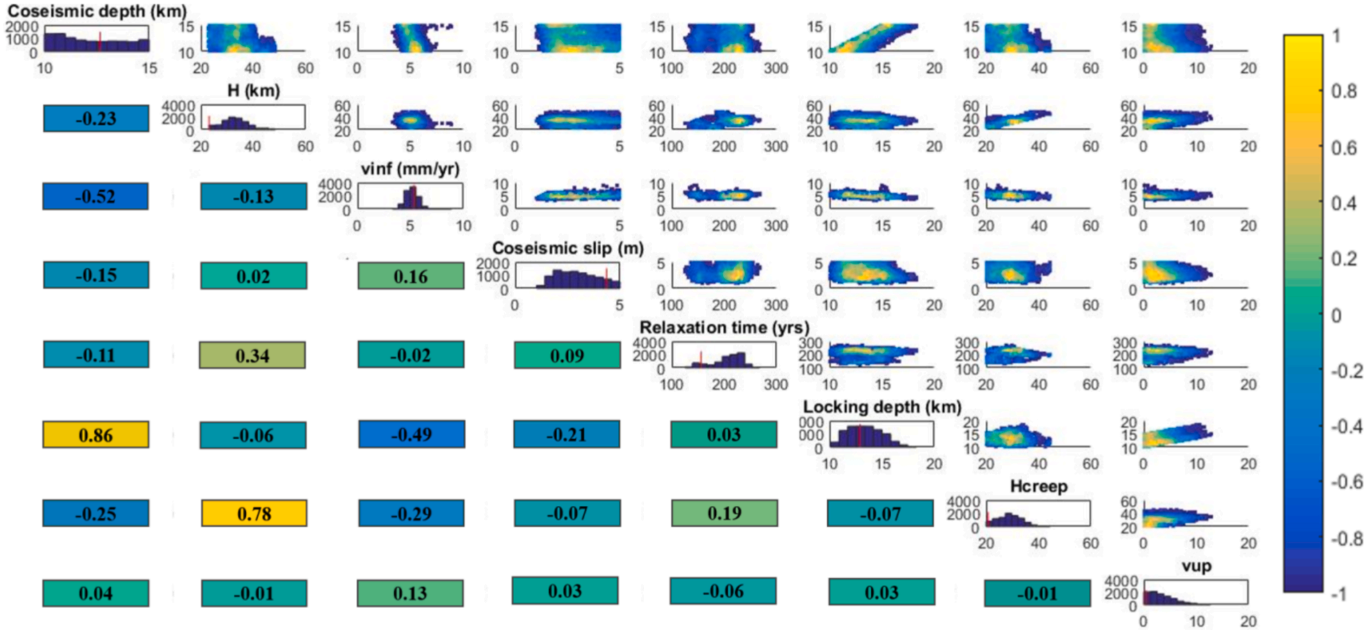

Fig. 15. Marginal posterior distributions and extracted correlation values for estimated parameters from combining the forward problem and propagating creep inversion process using (Djamour et al. 2011) data. The best fit solution is shown with red lines. (For interpretation of the references to color in this figure legend, the reader is referred to the web version of this article.)

CRediT authorship contribution statement

Milad Salmanian: Writing – review & editing, Writing – original draft, Validation, Software, Methodology, Investigation, Formal analysis, Data curation, Conceptualization. **Asghar Rastbood:** Writing – review & editing, Visualization, Validation, Supervision, Software. **Masoud Mashhadi Hossainali:** Writing – review & editing, Visualization, Supervision.

Author contribution

Only the authors mentioned in the paper contributed to this paper and there were no other contributors. All authors contributed to the study conception and design. Material preparation, data collection and analysis were performed by Milad Salmanian, Asghar Rastbood and Masoud Mashhadi Hossainali. The first draft of the manuscript was written by Milad Salmanian and all authors commented on previous versions of the manuscript. All authors read and approved the final manuscript. The authors have not received funding or financial assistance from any organization.

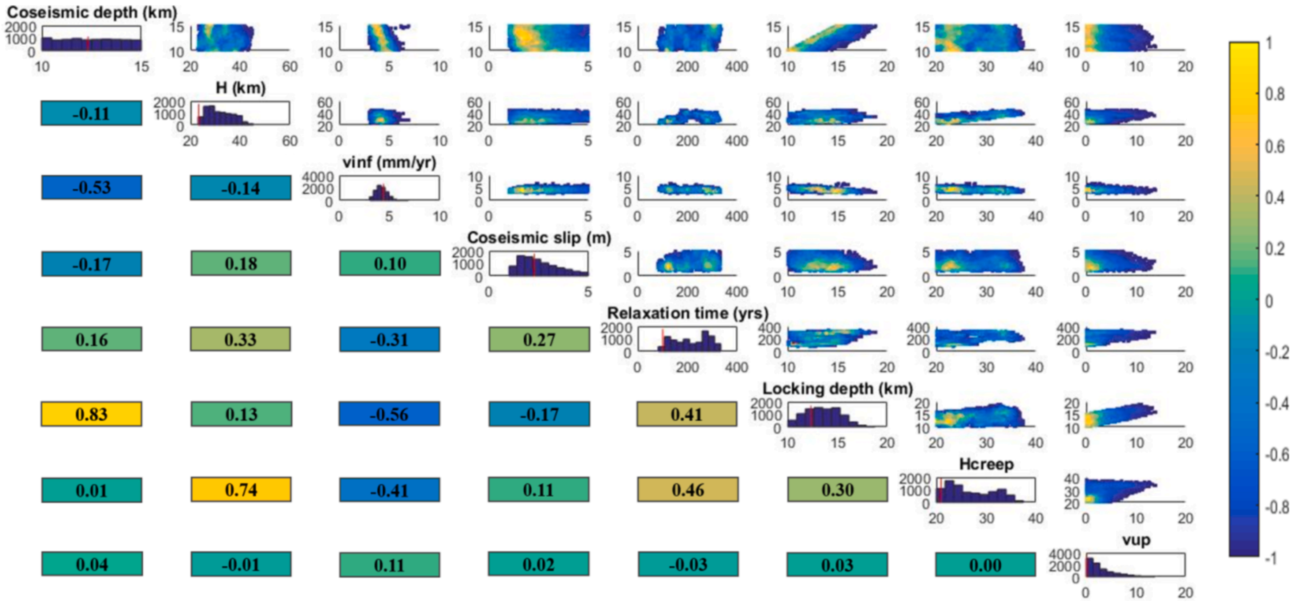

Fig. 16. Marginal posterior distributions and extracted correlation values for estimated parameters from combining the forward problem and propagating creep inversion process using (Haji-Aghajany et al. 2019) data. The best fit solution is shown with red lines. (For interpretation of the references to color in this figure legend, the reader is referred to the web version of this article.)

Declaration of competing interest

The authors declare that they have no known competing financial interests or personal relationships that could have appeared to influence the work reported in this paper.

Appendix A

Marginal posterior distributions and extracted correlation values for the eight parameters derived from the combination of the forward problem and propagating creep inversion process for an additional set of five chosen investigations are visually depicted in Figs. 12 to 16.

Data availability

Data will be made available on request.

References

Aghajany, S.H., Voosoghi, B., Yazdian, A., 2017. Estimation of north Tabriz fault parameters using neural networks and 3D tropospherically corrected surface displacement field: Geomatics. Nat. Haz. Risk 8 (2), 918–932.

Ambraseys, N.N., Melville, C.P., 2005. A history of Persian earthquakes. Cambridge University Press.

Aslan, G., Lasserre, C., Cakir, Z., Ergintav, S., Özarpaci, S., Dogan, U., Bilham, R., Renard, F., 2019. Shallow creep along the 1999 Izmit Earthquake rupture (Turkey) from GPS and high temporal resolution interferometric synthetic aperture radar data (2011–2017). J. Geophys. Res. Solid Earth 124 (2), 2218–2236.

Azad, S.S., Philip, H., Dominguez, S., Hessami, K., Shahpasandzadeh, M., Foroutan, M., Tabassi, H., Lamothe, M., 2015. Paleoseismological and morphological evidence of slip rate variations along the North Tabriz fault (NW Iran). Tectonophysics v. 640, 20–38.

Berberian, M., Arshadi, S., 1976. On the evidence of the youngest activity of the North Tabriz Fault and the seismicity of Tabriz city: Geol. Surv. Iran Rep 39, 397–418.

Berberian, M., Yeats, R.S., 1999. Patterns of historical earthquake rupture in the Iranian Plateau: Bulletin of the Seismological society of. America 89 (1), 120–139.

Berberian, M., 1994, Natural hazards and the first earthquake catalogue of Iran, International Institute of Earthquake Engineers and Seismology.

Berberian, M., 1997, Seismic sources of the Transcaucasian historical earthquakes: Historical and prehistorical earthquakes in the Caucasus, v. 28, p. 233-311.

Bruhat, L., 2020. A physics-based approach of deep interseismic creep for viscoelastic strike-slip earthquake cycle models. Geophys. J. Int. 220 (1), 79–95.

Bruhat, L., Segall, P., 2016. Coupling on the northern Cascadia subduction zone from geodetic measurements and physics-based models. J. Geophys. Res. Solid Earth 121 (11), 8297–8314.

Bruhat, L., Segall, P., 2017. Deformation rates in northern Cascadia consistent with slow updip propagation of deep interseismic creep. Geophys. J. Int. 211 (1), 427–449.

Bürgmann, R., 2018. The geophysics, geology and mechanics of slow fault slip. Earth Planet. Sci. Lett. 495, 112–134.

Confal, J.M., Bezada, M.J., Eken, T., Faccenda, M., Saygin, E., Taymaz, T., 2020. Influence of upper mantle anisotropy on isotropic P-wave tomography images obtained in the Eastern Mediterranean region. J. Geophys. Res. Solid Earth 125 (8) pp. e2019JB018559.

Djamour, Y., Vernant, P., Nankali, H.R., Tavakoli, F., 2011. NW Iran-Eastern Turkey Present-Day Kinematics: Results from the Iranian Permanent GPS Network. Earth Planet. Sci. Lett. 307 (1–2), 27–34.

Fialko, Y., 2006. Interseismic strain accumulation and the earthquake potential on the southern San Andreas fault system. Nature 441 (7096), 968–971.

Fichtner, A., Trampert, J., Cupillard, P., Saygin, E., Taymaz, T., Capdeville, Y., Villasenor, A., 2013. Multiscale full waveform inversion. Geophys. J. Int. 194 (1), 534–556.

Flück, P., Hyndman, R., Wang, K., 1997. Three-dimensional dislocation model for great earthquakes of the Cascadia subduction zone. J. Geophys. Res. Solid Earth 102 (B9), 20539–20550.

Foroutan, M., Meyer, B., Sébrier, M., Nazari, H., Murray, A., Le Dortz, K., Shokri, M., Arnold, M., Aumaître, G., Bourlès, D., 2014. Late Pleistocene-Holocene right slip rate and paleoseismology of the Nayband fault, western margin of the Lut block, Iran. J. Geophys. Res. Solid Earth 119 (4), 3517–3560.

Garfunkel, Z., 2015. The relations between Gondwana and the adjacent peripheral Cadomian domain—constrains on the origin, history, and paleogeography of the peripheral domain. Gondw. Res. 28 (4), 1257–1281.

Garthwaite, M.C., Wang, H., Wright, T.J., 2013. Broadscale interseismic deformation and fault slip rates in the central Tibetan Plateau observed using InSAR. J. Geophys. Res. Solid Earth 118 (9), 5071–5083.

Gomberg, J., Ellis, M., 1994. Topography and tectonics of the central New Madrid seismic zone: Results of numerical experiments using a three-dimensional boundary element program. J. Geophys. Res. Solid Earth 99 (B10), 20299–20310.

Gudmundsson, S., Sigmundsson, F., Carstensen, J.M., 2002. Three-dimensional surface motion maps estimated from combined interferometric synthetic aperture radar and GPS data. J. Geophys. Res. Solid Earth v. 107, no. B10 p. ETG 13–11-ETG 13–14.

Haji-Aghajany, S., Voosoghi, B., Amerian, Y., 2019. Estimating the slip rate on the north Tabriz fault (Iran) from InSAR measurements with tropospheric correction using 3D ray tracing technique. Adv. Space Res. 64 (11), 2199–2208.

Hessami, K., Pantosti, D., Tabassi, H., Shabanian, E., Abbassi, M. R., Feghhi, K., and Solaymani, S., 2003, Paleoearthquakes and slip rates of the North Tabriz Fault, NW Iran: preliminary results: Annals of Geophysics.

Hu, J., Liu, M., Taymaz, T., Ding, L., Irmak, T.S., 2024. Characteristics of strong ground motion from the 2023 Mw 7.8 and Mw 7.6 Kahramanmaraş earthquake sequence. Bull. Earthq. Eng. 1–30.

Hussain, E., Wright, T.J., Walters, R.J., Bekaert, D.P., Lloyd, R., Hooper, A., 2018. Constant strain accumulation rate between major earthquakes on the North Anatolian Fault. Nat. Commun. 9 (1), 1392.

Jackson, J., 1992. Partitioning of strike-slip and convergent motion between Eurasia and Arabia in eastern Turkey and the Caucasus. J. Geophys. Res. Solid Earth 97 (B9), 12471–12479.

Jackson, J., Ambraseys, N., Giardini, D., Balassanian, S., 1997. Convergence between Eurasia and Arabia in Eastern Turkey and the Caucasus: Historical and Prehistorical Earthquakes in the Caucasus v. 28, 79–90.

Jia, Z., Jin, Z., Marchandon, M., Ulrich, T., Gabriel, A.-A., Fan, W., Shearer, P., Zou, X., Rekoske, J., Bulut, F., 2023. The complex dynamics of the 2023 Kahramanmaraş, Turkey, M w 7.8-7.7 earthquake doublet. Science 381 (6661), 985–990.

Jiang, J., Lapusta, N., 2016. Deeper penetration of large earthquakes on seismically quiescent faults. Science 352 (6291), 1293–1297.

Karakhanian, A.S., Trifonov, V.G., Philip, H., Avagyan, A., Hessami, K., Jamali, F., Bayraktutan, M.S., Bagdassarian, H., Arakelian, S., Davtian, V., 2004. Active faulting and natural hazards in Armenia, eastern Turkey and northwestern Iran. Tectonophysics 380 (3–4), 189–219.

Karimzadeh, S., Cakir, Z., Osmanoğlu, B., Schmalzle, G., Miyajima, M., Amiraslanzadeh, R., Djamour, Y., 2013. Interseismic strain accumulation across the North Tabriz Fault (NW Iran) deduced from InSAR time series. J. Geodyn. 66, 53–58.

Khodaverdian, A., Zafarani, H., Rahimian, M., 2015. Long term fault slip rates, distributed deformation rates and forecast of seismicity in the Iranian Plateau. Tectonics 34 (10), 2190–2220.

Khorrami, F., Vernant, P., Masson, F., Nilfouroushan, F., Mousavi, Z., Nankali, H., Saadat, S.A., Walpersdorf, A., Hosseini, S., Tavakoli, P., 2019. An up-to-date crustal deformation map of Iran using integrated campaign-mode and permanent GPS velocities. Geophys. J. Int. 217 (2), 832–843.

Liu, C., Lay, T., Wang, R., Taymaz, T., Xie, Z., Xiong, X., Irmak, T.S., Kahraman, M., Erman, C., 2023. Complex multi-fault rupture and triggering during the 2023 earthquake doublet in southeastern Türkiye. Nat. Commun. 14 (1), 5564.

Mavrommatis, A.P., Segall, P., Uchida, N., Johnson, K.M., 2015. Long-term acceleration of aseismic slip preceding the Mw 9 Tohoku-oki earthquake: Constraints from repeating earthquakes. Geophys. Res. Lett. 42 (22), 9717–9725.

McKenzie, D., 1976. The East Anatolian Fault: a major structure in eastern Turkey. Earth Planet. Sci. Lett. 29 (1), 189–193.

Melgar, D., Ganas, A., Taymaz, T., Valkaniotis, S., Crowell, B.W., Kapetanidis, V., Tsironi, V., Yolsal-Çevikbilen, S., Öcalan, T., 2020. Rupture kinematics of 2020 January 24 M w 6.7 Doğanyol-Sivrice, Turkey earthquake on the East Anatolian Fault Zone imaged by space geodesy. Geophys. J. Int. 223 (2), 862–874.

Moradi, A.S., Hatzfeld, D., Tatar, M., 2011. Microseismicity and seismotectonics of the North Tabriz fault (Iran). Tectonophysics 506 (1–4), 22–30.

Nijholt, N., Simons, W., Efendi, J., Sarsito, D., and Riva, R., 2021, A transient in surface motions dominated by deep afterslip subsequent to a shallow supershear earthquake: The 2018 Mw7. 5 Palu Case: Geochemistry, Geophysics, Geosystems, v. 22, no. 4, p. e2020GC009491.

Okada, Y., 1985. Surface deformation due to shear and tensile faults in a half-space: Bulletin of the seismological society of. America 75 (4), 1135–1154.

Rizza, M., Vernant, P., Ritz, J., Peyret, M., Nankali, H., Nazari, H., Djamour, Y., Salamati, R., Tavakoli, F., Chery, J., 2013. Morphotectonic and geodetic evidence for a constant slip-rate over the last 45 kyr along the Tabriz fault (Iran). Geophys. J. Int. 193 (3), 1083–1094.

Salmanian, M., Rastbood, A., and Mashhadi Hossainali, M., 2024b, Stress Field Inversion Analysis of Earthquake Focal Mechanisms in Northwestern Iran: Implications for Tectonic Regimes: Journal of the Earth and Space Physics, v. 49, no. 4.

Salmanian, M., Rastbood, A., Mashhadi Hossainali, M., 2024a. Estimating the slip rate in the North Tabriz Fault using focal mechanism data and GPS velocity field. J. Geodetic Sci.

Savage, J., Burford, R., 1970. Accumulation of tectonic strain in California. Bull. Seismol. Soc. Am. 60 (6), 1877–1896.

Savage, J., Prescott, W., 1978. Asthenosphere readjustment and the earthquake cycle. J. Geophys. Res. Solid Earth 83 (B7), 3369–3376.

Scholz, C.H., 1998. Earthquakes and Friction Laws: Nature 391 (6662), 37–42.

Segall, P., 2010. Earthquake and volcano deformation. Princeton University Press.

Segall, P., Bradley, A.M., 2012. Slow-slip evolves into megathrust earthquakes in 2D numerical simulations. Geophys. Res. Lett. v. 39, no. 18.

Taymaz, T., Eyidoğan, H., and Jackson, J., 1991, Source parameters of large earthquakes in the East Anatolian Fault Zone (Turkey): Geophys. J. Int. v. 106, no. 3, p. 537-550.

Taymaz, T., Ganas, A., Yolsal-Çevikbilen, S., Vera, F., Eken, T., Erman, C., Keleş, D., Kapetanidis, V., Valkaniotis, S., Karasante, I., 2021. Source Mechanism and Rupture Process of the 24 January 2020 Mw 6.7 Doğanyol-Sivrice Earthquake obtained from Seismological Waveform Analysis and Space Geodetic Observations on the East Anatolian Fault Zone (Turkey). Tectonophysics 804. TECTO14240-228745.

Taymaz, T., Ganas, A., Berberian, M., Eken, T., Irmak, T.S., Kapetanidis, V., Yolsal-Çevikbilen, S., Erman, C., Keleş, D., Esmaeili, C., 2022. The 23 February 2020 Qotur-Ravian earthquake doublet at the Iranian-Turkish border: Seismological and InSAR evidence for escape tectonics. Tectonophysics v. 838, 229482.

Vernant, P., Nilforoushan, F., Hatzfeld, D., Abbassi, M., Vigny, C., Masson, F., Nankali, H., Martinod, J., Ashtiani, A., Bayer, R., 2004. Present-day crustal deformation and plate kinematics in the Middle East constrained by GPS measurements in Iran and northern Oman. Geophys. J. Int. 157 (1), 381–398.

Wang, H., Huang, Z., Eken, T., Keleş, D., Kaya-Eken, T., Confal, J.M., Erman, C., Yolsal-Çevikbilen, S., Zhao, D., Taymaz, T., 2020. Isotropic and anisotropic P wave velocity structures of the crust and uppermost mantle beneath Turkey. J. Geophys. Res. Solid Earth 125 (12) pp. e2020JB019566.

Wang, Z., Zhang, W., Taymaz, T., He, Z., Xu, T., Zhang, Z., 2023. Dynamic rupture process of the 2023 Mw 7.8 Kahramanmaraş earthquake (SE Türkiye): Variable rupture speed and implications for seismic hazard. Geophys. Res. Lett. 50 (15) pp. e2023GL104787.

Zhang, Y., Tang, X., Liu, D., Taymaz, T., Eken, T., Guo, R., Zheng, Y., Wang, J., Sun, H., 2023. Geometric controls on cascading rupture of the 2023 Kahramanmaraş earthquake doublet. Nat. Geosci. 16 (11), 1054–1060.